Cell Reports

Article

A Brainstem Locomotor Circuit Drives the Activity of Speed Cells in the Medial Entorhinal Cortex

Graphical Abstract

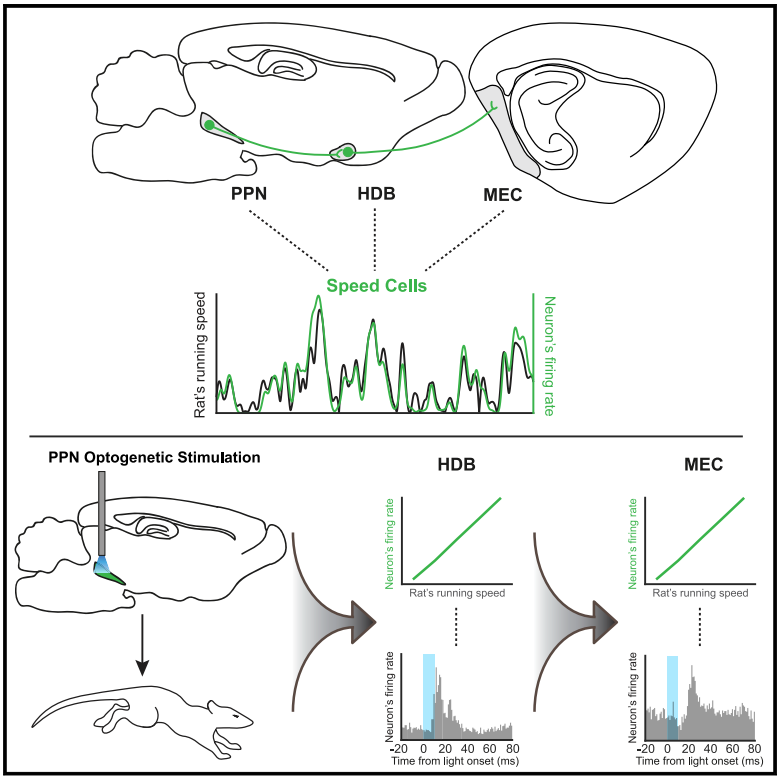

Highlights

- A speed-coding multisynaptic circuit connects PPN to MEC via HDB
- Each level of the PPN-HDB-MEC pathway contains cells with linear speed coding
- Optogenetic stimulation of PPN elicits activity in HDB and MEC speed cells
- In MEC, locomotor inputs from PPN mainly target speed-modulated interneurons

Authors

Miguel M. Carvalho, Nouk Tanke, Emilio Kropff, Menno P. Witter, May-Britt Moser, Edvard I. Moser

Correspondence

edvard.moser@ntnu.no

In Brief

Carvalho et al. describe a brain circuit in rats that conveys information about locomotion speed from the brainstem to cortical structures implicated in navigation. Optogenetic activation of the brainstem's pedunculopontine nucleus drives locomotion and modulates speed-modulated neurons in the diagonal band of Broca and the medial entorhinal cortex.

Carvalho et al., 2020, Cell Reports *32*, 108123
September 8, 2020
https://doi.org/10.1016/j.celrep.2020.108123

CellPress

Cell Reports

CellPress
OPEN ACCESS

Article

A Brainstem Locomotor Circuit Drives the Activity of Speed Cells in the Medial Entorhinal Cortex

Miguel M. Carvalho,[1,3] Nouk Tanke,[1,3,4] Emilio Kropff,[2] Menno P. Witter,[1] May-Britt Moser,[1] and Edvard I. Moser[1,5,*]

[1]Kavli Institute for Systems Neuroscience and Centre for Neural Computation, Norwegian University of Science and Technology, Olav Kyrres Gate 9, 7491 Trondheim, Norway

[2]Leloir Institute, IIBBA – CONICET, Av. Patricias Argentinas 435, Buenos Aires CP C1405BWE, Argentina

[3]These authors contributed equally

[4]Present address: Donders Institute for Brain, Cognition and Behavior, Radboud University Medical Centre, Heyendaalseweg 135, 6525 AJ Nijmegen, the Netherlands

[5]Lead Contact

*Correspondence: edvard.moser@ntnu.no

https://doi.org/10.1016/j.celrep.2020.108123

SUMMARY

Locomotion activates an array of sensory inputs that may help build the self-position map of the medial entorhinal cortex (MEC). In this map, speed-coding neurons are thought to dynamically update representations of the animal's position. A possible origin for the entorhinal speed signal is the mesencephalic locomotor region (MLR), which is critically involved in the activation of locomotor programs. Here, we describe, in rats, a circuit connecting the pedunculopontine tegmental nucleus (PPN) of the MLR to the MEC via the horizontal limb of the diagonal band of Broca (HDB). At each level of this pathway, locomotion speed is linearly encoded in neuronal firing rates. Optogenetic activation of PPN cells drives locomotion and modulates activity of speed-modulated neurons in HDB and MEC. Our results provide evidence for a pathway by which brainstem speed signals can reach cortical structures implicated in navigation and higher-order dynamic representations of space.

INTRODUCTION

In the mammalian brain, the medial entorhinal cortex (MEC) and the hippocampus are part of a dedicated neuronal network that allows an animal to create an internal representation of its current position by continuously integrating self-motion cues as the animal traverses the environment (McNaughton et al., 1996; 2006; Moser et al., 2014). This process, known as path integration (Mittelstaedt and Mittelstaedt, 1980; Gallistel, 1990; Etienne and Jeffery, 2004), provides a mechanism for translating activity across the internal spatial representation in accordance with the animal's changing location. A key component of this self-position system is the network of grid cells in the MEC (Fyhn et al., 2004; Hafting et al., 2005), whose multiple spatially confined firing fields form a hexagonal lattice across the entire environment. Because the relative position of firing fields of different grid cells is maintained across environments and behavioral tasks (Fyhn et al., 2007; Yoon et al., 2013), self-motion, rather than external sensory inputs, may determine grid cell firing in moving animals (McNaughton et al., 2006; Moser et al., 2014). A path integration-based mechanism for translation is further supported by the fact that passive transport disrupts the spatial regularity of grid cells (Winter et al., 2015b), whereas in virtual environments, grid cells respond to changes in the gain between locomotion and translation of the visual scene (Campbell et al., 2018). Similarly, in place cells, the firing fields are often controlled by the animal's movement when translocation is decoupled from the animal's ambulation (Gothard et al., 1996; Czurkó et al., 1999; Redish et al., 2000; Terrazas et al., 2005; Chen et al., 2013; Ravassard et al., 2013). These observations support the notion that active self-motion is necessary for spatially responsive cells in MEC and hippocampus to keep track of the animal's location (McNaughton et al., 1996, 2006; Fuhs and Touretzky, 2006; Burgess et al., 2007; Hasselmo et al., 2007; Burak and Fiete, 2009).

Path integration requires information about the animal's ongoing speed. Such information is expressed in specialized MEC cells referred to as speed cells (Kropff et al., 2015; Ye et al., 2018), although some cells also encode speed conjunctively with positional or directional correlates (Sargolini et al., 2006; Hinman et al., 2016; Hardcastle et al., 2017). Speed is also expressed in place cells of the hippocampus (McNaughton et al., 1983; Wiener et al., 1989; Czurkó et al., 1999). The linear relationship between speed and the firing rate of most MEC speed cells allows direct temporal integration of the animal's displacement and so provides a self-motion-derived signal that dynamically updates firing in grid cells (Kropff et al., 2015). However, locomotor speed may also be encoded non-linearly in some MEC cells (Hinman et al., 2016).

The emergence of the speed cell signal in MEC remains poorly understood, although several studies have pointed to a subcortical origin. Speed-correlated firing may reflect the activity of

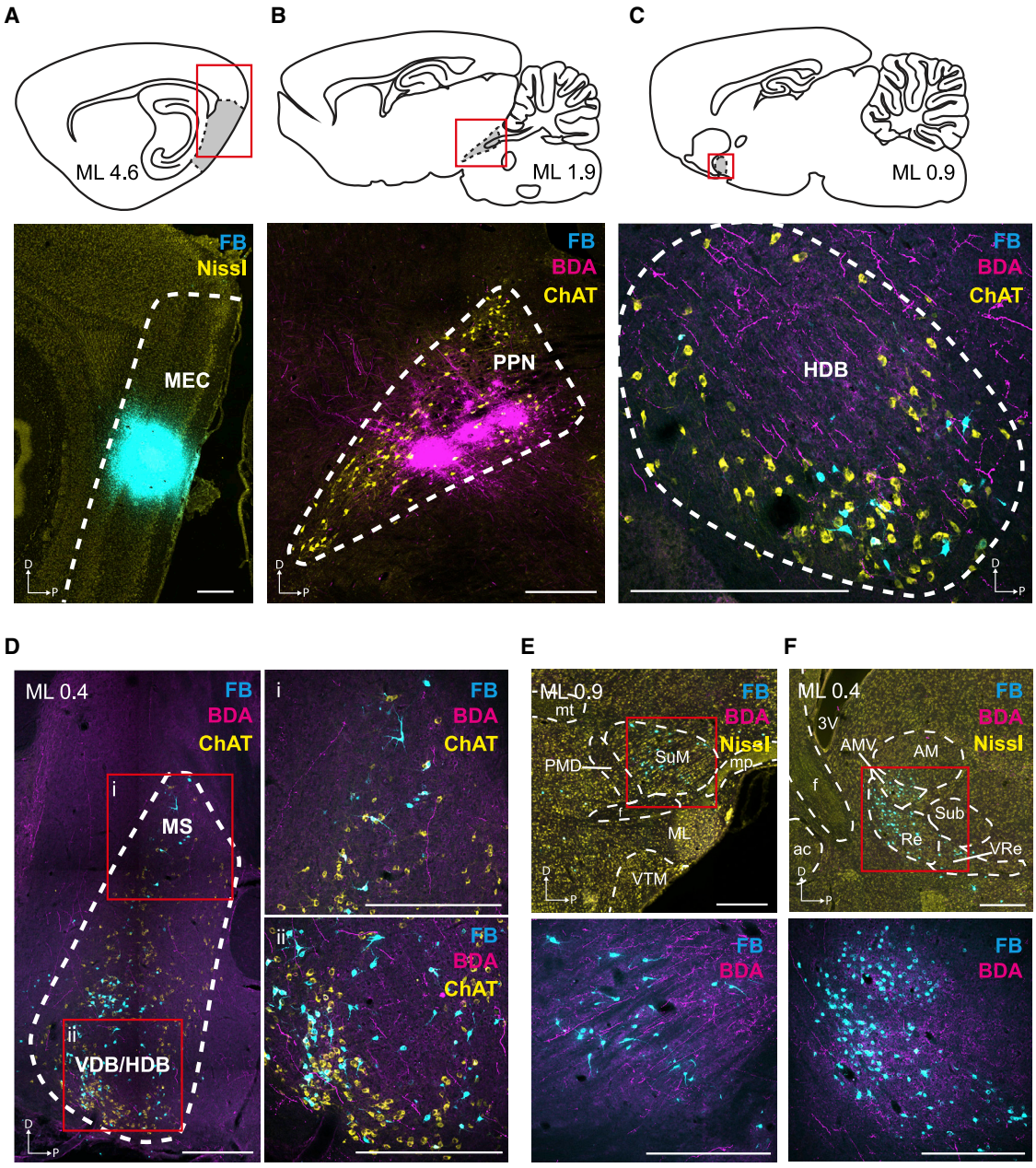

Figure 1. Anatomical Connectivity between PPN and MEC

(A–C) Top row: sagittal sections showing schematic of target areas for tracer injections (gray). Red rectangles indicate location of respective panels in lower row.

(A) Injection of retrograde tracer fast blue (FB) in MEC (white dashed line) with fluorescent Nissl counterstaining. The injection spans all cortical layers.

(B) Injection of the anterograde tracer biotinylated dextran amine (BDA) in PPN in the same animal as in (A). Anatomical boundaries of PPN (white dashed line) defined by choline acetyltransferase (ChAT) immunofluorescence staining. Note the absence of FB-labeled neurons in PPN.

(C) Overlap between PPN axonal projections (BDA) and MEC-projecting neurons (FB) in HDB (white dashed line), as defined by ChAT immunofluorescence staining. In addition to the presence of PPN projections outside HDB, note the substantial amount of labeled axons within the anatomical borders of HDB, some of which close to MEC-projecting FB-labeled neurons (see Dii for further evidence of double-labeling proximity).

(D–F) Additional brain areas displaying double BDA and FB staining.

(D) Left: BDA/FB labeling along the dorsoventral axis of the medial septum, vertical and horizontal limbs of the diagonal band region (MS, VDB, HDB, white dashed line, boundary defined by ChAT immunofluorescence staining, different case than A–C). Red squares represent high-magnification regions of interest (ROIs) shown to the right, displaying BDA/FB staining, respectively, in MS (i) and HDB and directly adjacent VDB (ii).

(legend continued on next page)

neurons in the medial septum and diagonal band of Broca (MSDB), a brain region that sends strong direct projections to both hippocampus and MEC (Amaral and Kurz, 1985; Gaykema et al., 1990; Unal et al., 2015; Fuchs et al., 2016) and that controls the dynamics of place cells in the hippocampus (Buzsáki, 2002; Colgin, 2016) and grid cells in the MEC (Brandon et al., 2011; Koenig et al., 2011) during active exploration. Because MSDB neurons with projections to MEC and CA1 are modulated by running speed (King et al., 1998; Fuhrmann et al., 2015; Justus et al., 2017), MSDB may play a role in implementing path integration in these target regions (Martin et al., 2007; Jacob et al., 2017).

However, the importance that active locomotion plays in the generation of stable and regular spatial codes in hippocampus and MEC suggests the need for these regions to be linked to brain circuits that directly participate in the onset of locomotor programs. Early studies of the mammalian brainstem showed that electrical stimulation of the mesencephalic locomotor region (MLR), a region composed of the cuneiform and the pedunculopontine nuclei (CnF and PPN, respectively), can elicit progressively faster gaits in a frequency-dependent manner (Shik et al., 1969; Skinner and Garcia-Rill, 1984; Garcia-Rill et al., 1987). More recently, optogenetic studies have shown that the locomotion-inducing role of MLR is under bidirectional control of basal ganglia output pathways and linked to activation of glutamatergic neurons in both CnF and PPN (Lee et al., 2014; Roseberry et al., 2016; Caggiano et al., 2018; Josset et al., 2018). Interestingly, different elements of the MLR circuit are tuned to different behavioral contexts, with CnF involved in escape responses and PPN implicated in exploratory behaviors (Caggiano et al., 2018). In addition to descending projections to spinal regions, the MLR sends widespread ascending projections to several thalamic, basal ganglia, and forebrain targets (Woolf and Butcher, 1986; Losier and Semba, 1993; Martinez-Gonzalez et al., 2011; Ryczko and Dubuc, 2013; Mena-Segovia and Bolam, 2017), with PPN serving as one of the main sources of projections to the MSDB area (Hallanger and Wainer, 1988). Activation of ascending MLR projections in cholinergic basal forebrain regions, including MSDB, has been shown to replicate activity states in primary visual cortex that are linked to locomotion, even in the absence of movement (Lee et al., 2014). Taken together, these findings point to the MLR as a possible modulator of locomotor-dependent cortical activity by way of its projections through the basal forebrain.

Here, we hypothesized that the MLR, and more specifically the PPN, serves as a brainstem source of locomotor-derived speed inputs that modulate the neuronal encoding of speed in MEC during exploration. Using a combination of anatomical tracing, *in vivo* single-unit recordings, and optogenetic stimulation, we describe here a neuronal circuit in the rat brain that by way of connections from PPN to the horizontal limb of the diagonal band of Broca (HDB), and further from HDB to MEC, controls the activity of speed cells in the MEC.

RESULTS

Anatomical Connectivity between MLR and MEC

To determine whether and how locomotion-related activity in MLR might influence speed coding in MEC, we started out by mapping the anatomical connections between these regions using neuronal tracers (Figure 1). We performed simultaneous injections of the retrograde tracer fast blue (FB) in dorsal MEC (n = 4 rats; Figure 1A; Figure S1A) and the anterograde tracer biotinylated dextran amine (BDA) in MLR, specifically targeting PPN (n = 4 rats; Figure 1B). No FB-labeled neurons were identified in PPN, suggesting an absence of monosynaptic projections from PPN to MEC (Figure 1B). A subsequent brain-wide tracer labeling analysis allowed us to identify several brain areas where it was possible to observe the co-occurrence of BDA-labeled axonal projections from PPN and FB-labeled neurons projecting to MEC. Such labeling was prominent in HDB and the border region between horizontal and vertical limbs of the diagonal band (Figures 1C and 1D). Even without direct evidence for monosynaptic connections between PPN and HDB, this result points to HDB as one of several potential relays for communication between PPN and MEC. Additional double labeling of BDA and FB was observed in the medial septum (MS; Figure 1D), supramammillary nucleus (SuM; Figure 1E), and nucleus reuniens (Re; Figure 1F), opening the possibility for multiple parallel pathways connecting PPN to MEC.

In addition to identifying the HDB region as a major convergence site between PPN and MEC, we sought to identify the source of HDB afferents from the nuclei within the MLR, specifically the CnF and the PPN (Ryczko and Dubuc, 2013), as this region is known to send projections to MSDB targets (Woolf and Butcher, 1986; Hallanger and Wainer, 1988). We performed a FB injection in HDB (Figure S1B; n = 1 rat) and observed that within MLR, a substantial population of FB-labeled neurons was present in PPN (Figure S1C), validating this brain area as the main source of MLR monosynaptic projections to HDB.

Neuronal Coding of Locomotion Speed in PPN, HDB, and MEC

We then asked whether locomotion speed was encoded at each step of the PPN-HDB-MEC pathway. Rats were implanted with tetrodes to target PPN (n = 12 rats), HDB (n = 20 rats), and MEC (n = 35 rats) (Figures 2A–2C; Figure S2). We performed single-unit recordings from these brain regions while the animals foraged for food crumbles in an open-field arena. On the basis of post hoc anatomical reconstruction of recording sites, we selected 1,890 units (PPN, n = 260 cells; HDB, n = 308 cells; MEC, n = 1,322 cells). In each area, we observed units where spike activity co-varied with the animal's running speed (Figures 2D–2F), most often by increasing or decreasing linearly with speed (Figures 2G–2I).

(E and F) Low-magnification (top) and high-magnification ROIs (red squares, bottom) showing BDA/FB labeling in the supramammillary nucleus (SuM) (E) and in the nucleus reuniens (Re) of the thalamus (F) (same case as in A–C).

ac, anterior commissure; AM, anteromedial thalamic nucleus; AMV, anteromedial thalamic nucleus, ventral part; f, fornix; ML, medial mammillary nucleus, lateral part; mp, mammillary peduncle; mt, mammillothalamic tract; PMD, premammillary nucleus, dorsal part; Sub, submedius thalamic nucleus; VRe, ventral reuniens thalamic nucleus; VTM, ventral tuberomammillary nucleus; 3V, third ventricle. Scale bars: 500 μm.

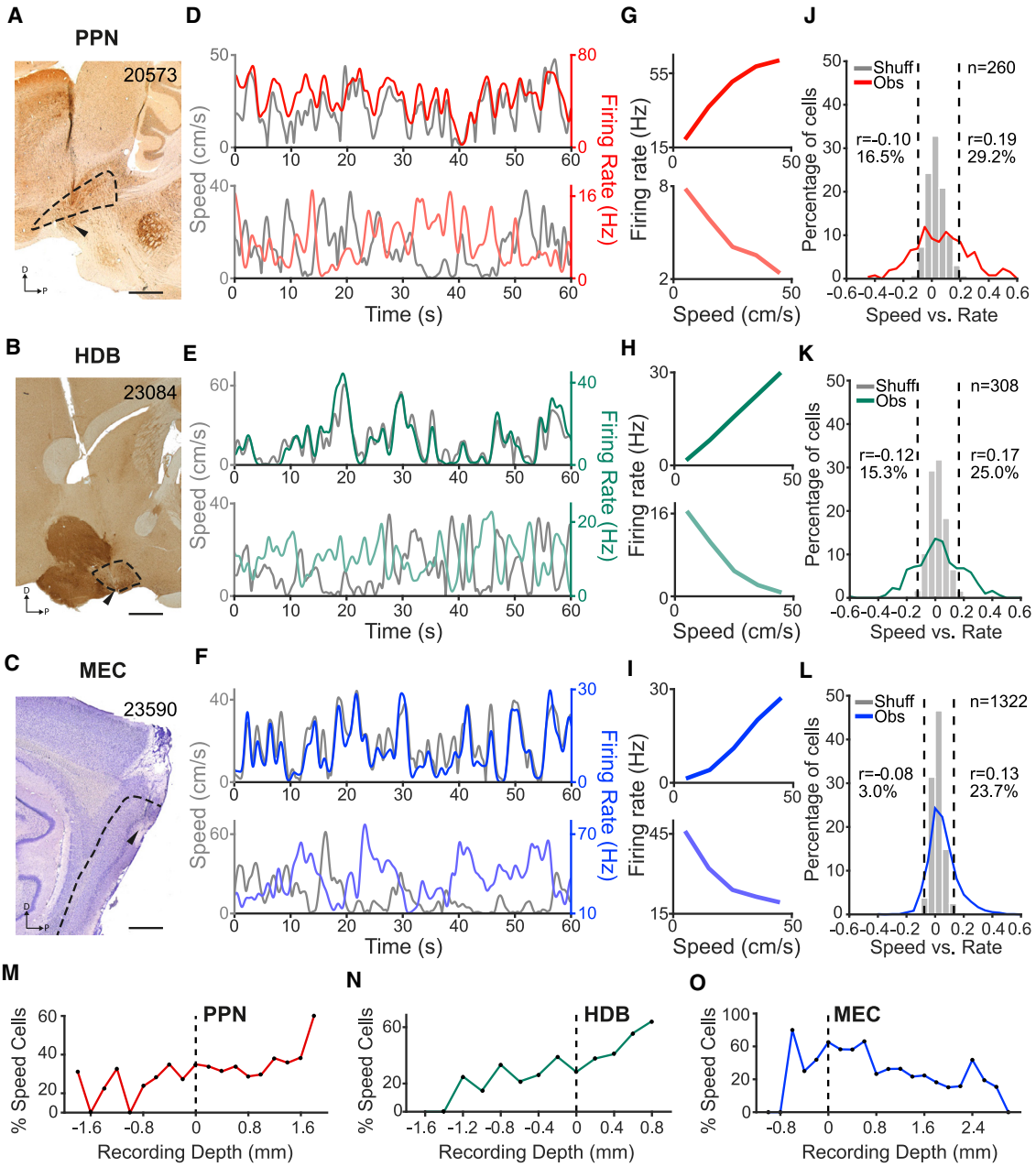

Figure 2. Neuronal Coding of Locomotion Speed in PPN, HDB, and MEC

(A–C) Sagittal sections showing representative tetrode tracks and anatomical boundaries of target recording sites for PPN (A), HDB (B), and MEC (C). Black arrowheads identify final (deepest) tetrode position. Rat numbers shown in top right corner. Scale bars: 1 mm.

(D–F) Covariance of firing rate (red, green, or blue line) with running speed (gray line) for one representative example of a positive (top) and a negative (bottom) speed cell in each region—PPN (D), HDB (E), and MEC (F)—sampled during 1 min of free foraging in the open field.

(G–I) Speed versus rate tuning curves for the speed cells shown in (D)–(F).

(J–L) Observed (Obs) and shuffled (Shuff) distributions of speed versus rate correlation values for units recorded within the boundaries of PPN (J), HDB (K), and MEC (L). Dashed lines indicate 1st and 99th percentiles of the shuffled distribution, which were used to classify units as negative or positive speed cells, respectively. Cell numbers, 1st and 99th percentile values (Pearson's r), and percentages of cells that passed criteria for each class of speed cells are indicated.

(M–O) Percentage of speed cells (positive and negative speed cells of all animals pooled together) as a function of recording depth (horizontal dashed line, 0 = dorsal boundary of the respective brain area) in each target region: brainstem (M), basal forebrain (N), and entorhinal cortex (O).

For every single unit in each area, we calculated a speed score—Pearson's correlation between the unit firing rate and the animal's running speed, considering only periods when running speed was between 6 cm/s and the mean value of the last 10 cm/s speed bin in which the animal had spent more than 30 s—and we classified units as negative or positive speed cells if their speed scores were lower than the 1st or higher than the 99th percentile of a shuffled distribution of observed speed versus rate values, respectively (Figures 2J–2L; Kropff et al., 2015). The speed threshold, modified from a previous report (Kropff et al., 2015), was chosen empirically to represent the approximate transition between discrete neural firing regimes in MEC (Figure S3A). At low speeds, from 0 to 6 cm/s, the firing rates of MEC cells increased sharply, likely as a result of network state changes following locomotor onset. Above 6 cm/s, firing increased with increasing locomotor speed in an apparently linear manner. The presence of two discrete firing regimes was also observed in PPN and HDB (Figure S3A), allowing us to remove from our further analyses in each brain region any behavioral-state effects associated with locomotor onset or arrest. During running, a linear speed cell signal in MEC, with monotonically increasing or decreasing speed tuning curves, may provide a more robust moment-by-moment account of the animal's running speed as required for path integration (Fuhs and Touretzky, 2006; McNaughton et al., 2006; Burgess et al., 2007; Hasselmo et al., 2007; Burak and Fiete, 2009). However, by classifying speed cells according to a linear model, we may undermine the identification of non-linear speed signals present in MEC (Hinman et al., 2016; Hardcastle et al., 2017) but also within MSDB (Zhou et al., 1999) and PPN (Caggiano et al., 2018). We therefore compared speed cell classification with linear and non-linear correlation measures (Pearson's and Spearman's correlations, respectively). With a 6 cm/s speed threshold, the two approaches revealed largely overlapping populations of speed cells in each brain region (PPN, 100 of 124 [81%]; HDB, 108 of 127 [85%]; MEC, 311 of 489 [64%]), suggesting that the vast majority of speed cells have a significant linear relationship to speed, although not excluding additional nonlinear components (see legend of Figure 3SB).

In PPN, 43 cells (16.5%) were classified as negative speed cells and 76 (29.2%) as positive speed cells. In HDB, 47 cells (15.3%) were classified as negative speed cells and 77 (25.0%) as positive speed cells. In MEC, 40 cells (3.0%) were classified as negative speed cells and 313 (23.7%) as positive speed cells, in agreement with previous observations implying predominantly positive speed relationships in MEC (Kropff et al., 2015). Speed-modulated cells were generally observed also in "off-target" recording sites surrounding the anatomical boundaries of PPN, HDB, and MEC (Figures 2M–2O; Figure S4). In MEC we also recorded grid cells (n = 119), head direction cells (n = 202), and border cells (n = 93), a small number of which also encoded locomotor speed, either positively (grid, n = 14; head direction, n = 23; border, n = 11) or negatively (grid, n = 1; head direction, n = 6; border, n = 11). The activity of the speed cells recorded in each brain area was tuned to either preceding or succeeding running speeds, within a range of a few hundred milliseconds (Figure S3C). In a previous study, a subset of positive speed cells in MEC displayed an overall prospective temporal bias in the encoding of running speed, with changes in firing rate anticipating changes in running speed (Kropff et al., 2015). This temporal bias was replicated in the present dataset (time shift for maximal average correlation 62.0 ms). A similar average prospective bias was observed for positive speed cells in HDB (time shift for maximal average correlation 128.7 ms). In the case of PPN, we observed no significant average temporal bias in the coding of locomotor speed in either positive or negative speed cells. Instead, there was a mixture of retrospective and prospective speed tuning, which was also observed in HDB and MEC, despite the overall prospective bias seen in positive speed cells (Figure S3C).

Optogenetic Stimulation of PPN Can Both Activate and Terminate Locomotor Activity

In order to determine how locomotor programs in PPN influence firing activity of downstream speed cells in HDB and MEC, we targeted PPN cells optogenetically. We started out by checking that PPN stimulation engages locomotion, as reported in early studies with broad electrical or optogenetic stimulation in MLR (Shik et al., 1969; Skinner and Garcia-Rill, 1984; Lee et al., 2014; Roseberry et al., 2016; Caggiano et al., 2018). Rats were injected unilaterally with a channelrhodopsin-2 (ChR2)-expressing adeno-associated virus (AAV) [AAV5-CaMKIIa-hChR2(H134R)-EYFP] in PPN, followed by the implantation of an optic fiber in the same location (n = 17 rats; Figure 3A). Simultaneously, these rats were implanted with tetrodes targeting HDB and/or MEC, allowing us to record downstream changes in the firing activity of speed cells in response to PPN laser stimulation.

We tested the effects of PPN laser stimulation on locomotion by delivering multiple 5 s trains of 10 ms laser pulses at 10 Hz frequency, separated by a 15 s pause, while the rats explored an open field. Consistent with previous optogenetic stimulation experiments in MLR (Lee et al., 2014; Roseberry et al., 2016; Caggiano et al., 2018), our stimulation protocol generally induced an abrupt increase in running speed (laser on from 0 to 5 s), compared with baseline (from −5 to 0 s) (baseline versus stimulation speed, $Z = 5.8$, $p = 5.9 \times 10^{-9}$, Wilcoxon signed-rank test; Figure 3B; Video S1). Robust locomotor activation was observed in the majority of ChR2-expressing rats (n = 13 of 17 rats; group baseline speed 10.3 ± 0.8 cm/s, group stimulation speed 30.3 ± 3.7 cm/s; $Z = 3.2$, $p = 1.5 \times 10^{-3}$, Wilcoxon signed-rank test; Figure 3C; Figure S5A). In a small number of ChR2-expressing rats (n = 4 of 17), locomotion was instantly slowed down or interrupted during the 5 s of PPN stimulation (baseline versus stimulation speed, $Z = 5.9$, $p = 3.1 \times 10^{-9}$, Wilcoxon signed-rank test; Figure 3D; group baseline speed 12.5 ± 2.6 cm/s, group stimulation speed 3.4 ± 0.8 cm/s; Figure S5B; Video S1). Regardless of the behavioral phenotype that was elicited, we observed that the changes in locomotor behavior following PPN optogenetic stimulation were consistent across recording sessions (Figures S5A and S5B; confirmation of optic fiber placements in Figure S5C). No changes in running speed were observed in a cohort of animals injected with a control virus (AAV5-CaMKIIa-EYFP; n = 4; Figures S5D–S5F).

PPN Stimulation Modulates Downstream Speed Cell Activity in HDB and MEC

Next, we evaluated how the activation of PPN motor programs affects the activity of speed cells in HDB and MEC in rats with

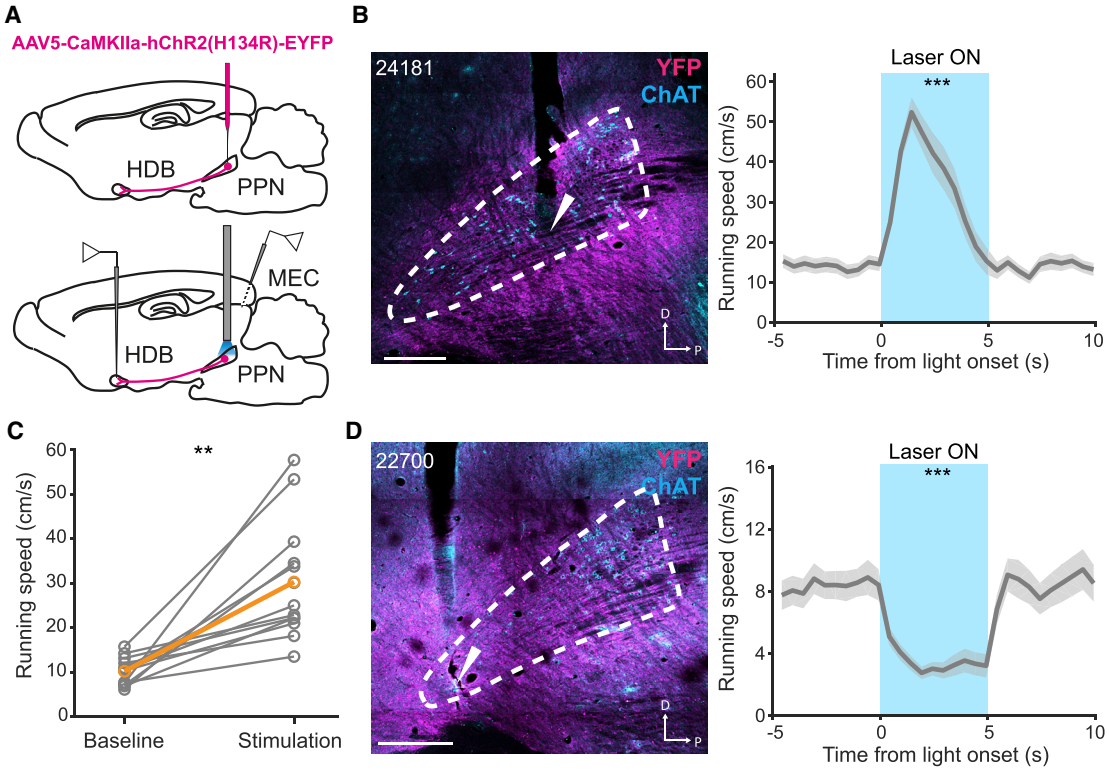

Figure 3. Optogenetic Stimulation of Brainstem Locomotor Circuits

(A) Schematic representation of PPN optogenetic stimulation experiments. After injection of AAV5-CaMKIIa-hChR2(H134R)-EYFP in PPN (top), animals were implanted with an optic fiber in PPN and tetrodes in HDB and MEC (bottom), in order to record activity of speed cells in the latter regions in response to PPN stimulation.

(B) Left: sagittal immunofluorescence photomicrograph of the brainstem of one representative ChR2-expressing animal (rat number shown in top left corner) implanted with an optic fiber in PPN (YFP expression in ChR2 neurons in magenta). The anatomical boundary of PPN (white dashed line) was defined with ChAT immunofluorescence staining (cyan). White arrows indicate tip of optic fiber. Right: increases of average running speed during PPN optogenetic stimulation (laser on, blue window) for the animal identified on the left. Gray line represents mean ± SEM running speed for all laser-on periods during one stimulation session.

(C) Individual (gray) and group-average (orange) running speed between baseline (−5 to 0 s, before laser onset) and stimulation (0 to 5 s, after laser onset) epochs for the 13 ChR2-expressing animals that responded with increases in running speed (speed values of each animal averaged over seven to ten stimulation sessions).

(D) Same as in (B), but for one of four animals that displayed reduced locomotion or freezing during PPN stimulation.

**$p < 0.01$ and ***$p < 0.001$, Wilcoxon signed-rank test between baseline and stimulation epochs. Scale bars: 500 μm.

dual tetrode implants in these areas, combined with an optic fiber in PPN. These experiments started with a 20–30 min open-field baseline session, in which we screened for single units in HDB and/or MEC. This was followed by a 10–20 min optogenetic stimulation session, during which we recorded the activity of HDB and MEC units in response to PPN stimulation (Figure 4A). During open-field exploration, PPN stimulation evoked transient and reliable absolute increases or decreases in firing rate in both positive and negative speed cells in HDB and MEC (Figure 4B; for criteria, see STAR Methods). Because downstream changes in HDB and MEC activity were observed independently of whether PPN stimulation elicited running or freezing (Figure S5G), data from all animals were used for further analyses.

Of the 162 units recorded in HDB of eight rats, 112 showed significant post-stimulus changes in firing rate following PPN stimulation (n = 54 excited, n = 58 inhibited; Figure 4C, top; for criteria, see STAR Methods). Of those responsive cells, 47 cells (42.0%) were classified as speed cells (Figure 4D, left; see Table S1 for results from individual animals). PPN-modulated speed cells represented 69.1% (47 of 68) of the whole population of speed cells recorded in HDB. Excitatory and inhibitory responses were observed in both positive and negative speed cells (positive speed cells: n = 13 excited, n = 12 inhibited; negative speed cells: n = 9 excited, n = 13 inhibited; Figure 4D, middle). In MEC, we recorded 366 units in 15 rats and found 71 responsive cells (n = 29 excited, n = 42 inhibited; Figure 4C, bottom). Of those responsive cells, 38 cells (53.5%) were classified as speed cells (Figure 4D, left; see Table S2 for results from individual animals), which represented 32.0% (38 of 119) of the whole population of speed cells recorded in MEC. As in HDB, excitatory and inhibitory responses could be observed in both positive and negative MEC speed cells (positive speed cells: n = 15 excited, n = 20 inhibited; negative speed cells: n = 1 excited, n = 2 inhibited; Figure 4D, middle). In both target regions, PPN stimulation affected firing also in cells with no speed

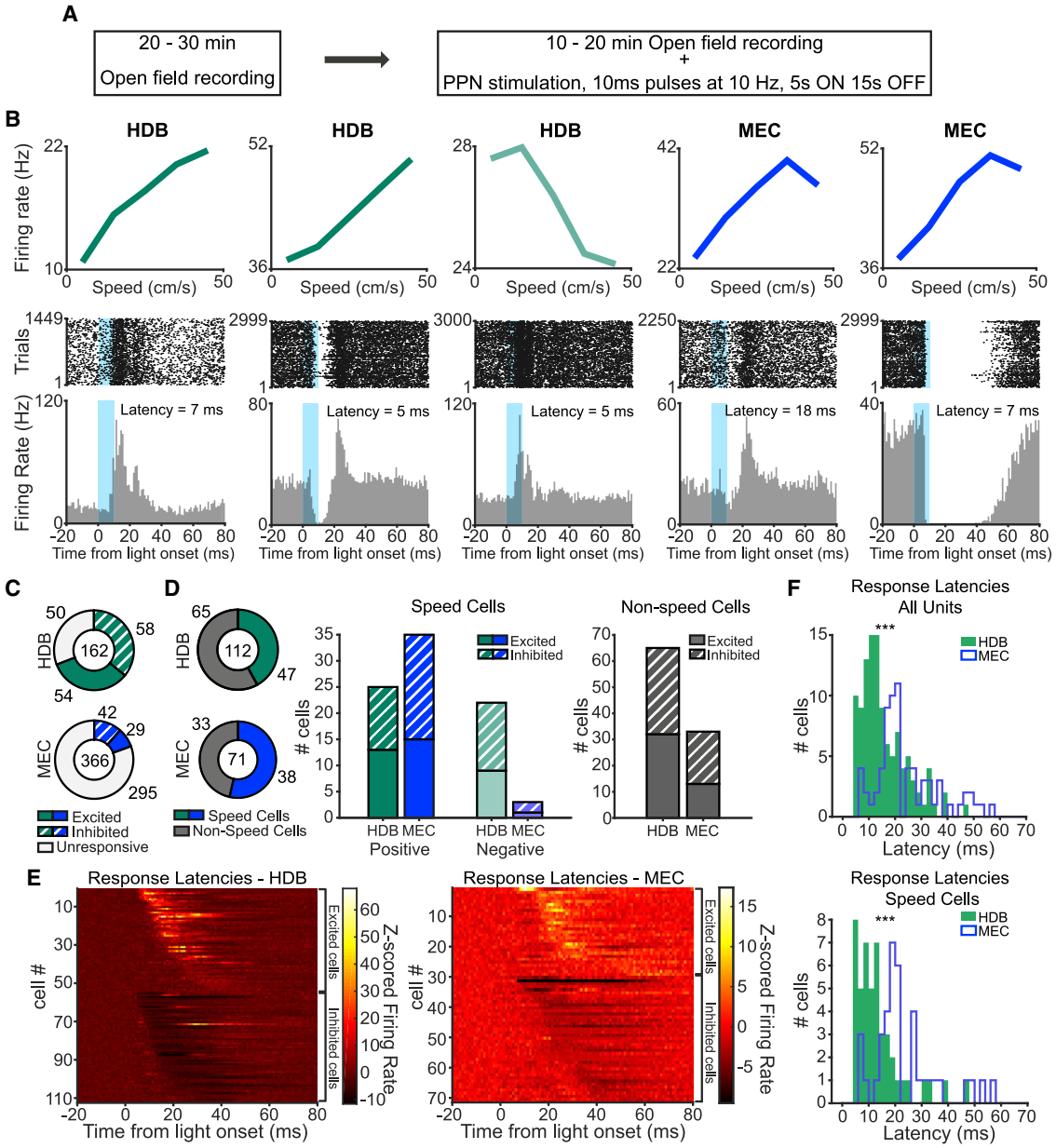

Figure 4. Cells in HDB and MEC Respond to Optogenetic Stimulation of PPN

(A) ChR2-expressing rats participated in two consecutive sessions in the open field: one baseline exploration and one stimulation session.

(B) Top row: examples of speed tuning curves (mean firing rate as a function of running speed) for two positive speed cells (two left panels) and one negative speed cell (middle panel) in HDB (green), and for two positive speed cells in MEC (right panels in blue), all recorded during the baseline session. Bottom row: corresponding raster plots (top) and peri-stimulus time histograms (bottom; PSTH, bins, 1 ms) for the respective speed cells shown in the top row. Absolute changes in firing rate are aligned to the onset of optogenetic laser pulses in PPN (blue windows) during the stimulation session. The cells in the second, third, and fifth rows have some of the shortest response latencies that were recorded in the HDB and MEC cell populations (all <10th percentile for the region). With local activation latencies of ~1 ms (Rowland et al., 2018), a latency of 7 ms from PPN stimulation to excitation or inhibition in MEC is likely compatible with a polysynaptic activation pathway from PPN, even if the pathway includes unmyelinated fibers.

(C) Total number of unresponsive (white), excited (filled), and inhibited (dashed) cells in HDB (top, green) and MEC (bottom, blue) following PPN stimulation. The total number of recorded cells is displayed in the center.

(D) Left: proportion of speed cells among all responsive cells in HDB (top, green) and MEC (bottom, blue) (sum of excited and inhibited cells in [C]). Middle: summary of numbers of responsive speed cells recorded in HDB (green) and MEC (blue) following PPN optogenetic stimulation, broken down by type of response (excitation, filled bars; inhibition, dashed bars) and speed cell class (positive speed cells, left bars; negative speed cells, right bars). Right: same as middle, but for all non-speed cells that were recorded in HDB (left) and MEC (right).

(legend continued on next page)

modulation (HDB: n = 32 excited, n = 33 inhibited; MEC: n = 13 excited, n = 20 inhibited; Figure 4D, right). Among non-speed cells, 69.1% (65 of 94) in HDB and 13.4% (33 of 247) in MEC were modulated by PPN stimulation.

A qualitative overview of the temporal dynamics of all responses to PPN stimulation revealed a broad span of response latencies in HDB and MEC (Figure 4E), although in general, the latencies reflected the cells' anatomical position along the proposed multisynaptic PPN-HDB-MEC circuit, with longer latencies in MEC than HDB (see STAR Methods). Median response latency for HDB cells was 13.0 ms and for MEC cells it was 20.0 ms (HDB, n = 112; MEC, n = 71; $Z = 5.4$, $p = 8.1 \times 10^{-8}$, Wilcoxon rank-sum test; Figure 4F, top). The difference between HDB and MEC latencies was maintained when analyses were restricted to speed cells (HDB: n = 47, median latency 11.0 ms; MEC: n = 38, median latency 19.5 ms; $Z = 4.6$, $p = 3.8 \times 10^{-6}$, Wilcoxon rank-sum test; Figure 4F, bottom). In both regions, responses were elicited well ahead of detectable changes in locomotion (see Figures 3B and 3D). Taken together, the results support a causal relationship between activation of locomotor programs in PPN and modulation of downstream speed cells in HDB and subsequently in MEC.

PPN Inputs Preferentially Target Speed-Modulated Putative Interneurons in MEC

To determine if any cell types in MEC were more likely to be targeted by PPN stimulation than others, we first classified MEC cells into putative principal cells (pPC) and putative interneurons (pINT) on the basis of firing rate and the bimodal distribution of spike widths for the entire sample of MEC units. Cells with a firing rate <10 Hz and a spike width >240 μs were classified as pPC and the rest of the population as pINT (Figure 5A; Figure S2). Using these criteria, we found that 16 of 206 (7.8%) pPC and 55 of 160 (34.4%) pINT in MEC were responsive to PPN stimulation, indicating a higher proportion of responsive cells among pINT than pPC ($Z = 6.4$, $p = 1.7 \times 10^{-10}$, two-proportions Z test; Figure 5B). Among all PPN-responsive MEC cells, 1 of 16 pPC (6.3%) and 37 of 55 (67.3%) pINT were classified as speed cells ($Z = 4.3$, $p = 1.7 \times 10^{-5}$, two-proportions Z test; Figure 5B), suggesting that speed-modulated pINT might be the preferential targets of PPN inputs. In line with this hypothesis, we observed a significantly larger number of responsive pINT than pPC within the entire subpopulation of speed cells recorded during PPN stimulation (n = 119; pPC, 1 of 39 [2.6%]; pINT, 37 of 80 [46.3%]; $Z = 4.8$, $p = 1.6 \times 10^{-6}$, two-proportions Z test), as well as within the entire subpopulation of non-speed cells (n = 247; pPC, 15 of 167 [9.0%]; pINT, 18 of 80 [22.5%]; $Z = 2.9$, $p = 3.5 \times 10^{-3}$, two-proportions Z test) (Figure 5C). Speed-modulated pINT were comparatively more responsive than non-speed-modulated pINT (speed-modulated pINT, 37 of 80 [46.3%]; non-speed-modulated pINT, 18 of 80 [22.5%]; $Z = 3.2$, $p = 1.6 \times 10^{-3}$, two-proportions Z test; Figure 5C). This difference was not observed for pPC (speed-modulated pPC, 1 of 39 [2.6%]; non-speed-modulated pPC, 15 of 167 [9.0%]; $Z = 1.4$, $p = 0.2$, two-proportions Z test).

Considering the plethora of functional cell types in MEC, we then wondered if other functional cell types in MEC also responded to the activation of motor programs in PPN. Compared with 38 of 119 (32.0%) responsive speed cells, 7 of 59 (11.9%) grid cells, 10 of 59 (17.0%) head direction cells, and 1 of 19 (5.7%) border cells showed stimulation-induced responses (Figure 5D; see Figures 5E and 5F for examples of responsive head direction and grid cells), indicating that responses to PPN stimulation were significantly more predominant in speed cells than in other functional populations (speed cells versus grid cells, $Z = 2.9$, $p = 3.7 \times 10^{-3}$; speed cells versus head direction cells, $Z = 2.1$, $p = 0.03$; speed cells versus border cells, $Z = 2.4$, $p = 0.017$; two-proportions Z-test). In sum, these results indicate that the downstream effects of PPN activation are non-uniformly distributed across functional cell types in MEC and appear to target preferentially pINT, in particular those that are speed modulated.

PPN Control of Speed Cell Activity in MEC Is Mediated via HDB

Given the existence of direct projections between PPN and HDB, as well as the ability of PPN to drive speed cell activity in HDB, and subsequently in MEC, we finally asked whether activation of HDB cells is sufficient for relaying locomotor-derived inputs from PPN to MEC. In a first experiment, we investigated the ability of PPN efferents in HDB to control speed cell activity in MEC. Animals injected with AAV5-CaMKIIa-hChR2(H134R)-EYFP in PPN were implanted with an optic fiber in HDB and tetrodes in MEC. Experiments with these animals consisted of a baseline recording session followed by a session in which single-unit activity was recorded in MEC while laser pulses were delivered to PPN axonal terminals in HDB (Figure 6A). Behaviorally, we observed significant changes in running speed during periods of optogenetic stimulation, consistent with our observations after stimulation within the PPN itself, albeit to a smaller degree (baseline speed 8.5 ± 0.4 cm/s, stimulation speed 11.2 ± 0.7 cm/s; $Z = 2.7$, $p = 6.9 \times 10^{-3}$, Wilcoxon signed-rank test; Figure 6B). In addition, we observed that activation of PPN terminals in HDB promoted changes in the firing activity of downstream speed cells in MEC (Figure 6C).

Among 161 recorded MEC units in five rats, we detected 1 inhibited cell and 16 cells that were excited in response to stimulation of PPN terminals in HDB. The majority of responsive cells were positively modulated speed cells (positive speed cells: n = 12 excited, n = 1 inhibited; negative speed cells: n = 1 excited; n = 0 inhibited; Figure 6D). These accounted for 25.5% (14 of 55) of the total of speed cells recorded in MEC. Responses to PPN terminal stimulation were also observed in non-speed cells (n = 3 excited, n = 0 inhibited; Figure 6D; 2.8% [3 of 106] of all non-speed MEC cells). Overall, we observed shorter response latencies following stimulation of PPN terminals in HDB than

(E) Color-coded summary of the changes in firing activity of all responsive cells in HDB (left panel) and MEC (right panel), ordered by response direction (excitation/inhibition) and response latency. Z-scored firing rate is color-coded (scale bar).
(F) Distributions showing response latencies in all responsive units (top) and all responsive speed cells (bottom) recorded in HDB (green) and MEC (blue). ***$p < 0.001$, Wilcoxon rank-sum test.

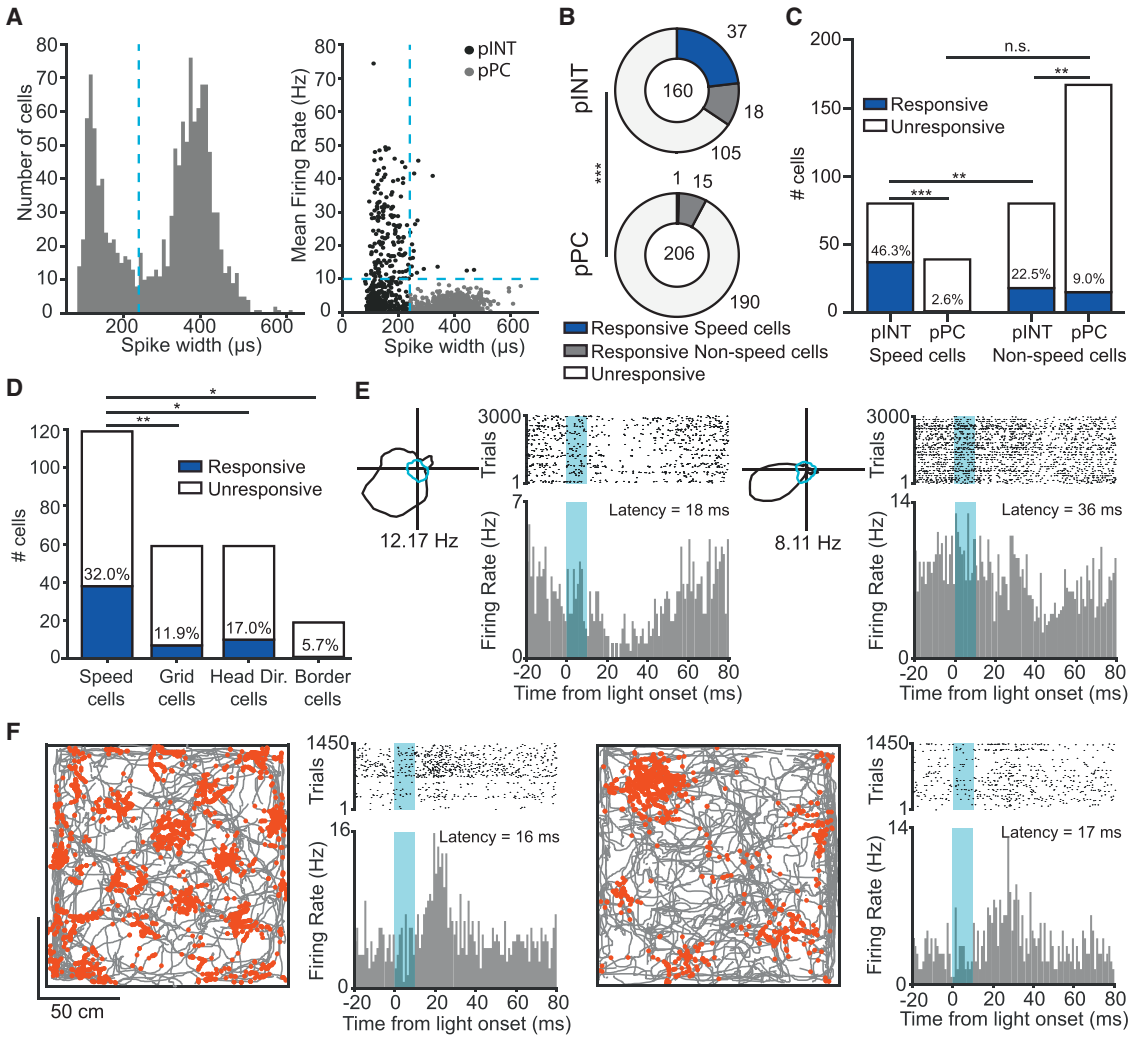

Figure 5. Non-uniform Targeting of PPN Inputs in MEC According to Cell Functional Properties

(A) Left: histogram of the distribution of spike widths for the entire population of recorded MEC cells. Note the clear bimodal distribution of spike widths with a minimum around the blue dashed line (spike width 240 μs) that indicates average between the two peak values and that was used to classify units as putative principal cells (pPC) and putative interneurons (pINT). Right: classification of MEC units according to spike width and firing rate criteria. Units with a spike width >240 μs and a firing rate <10 Hz were classified as pPC (gray dots), whereas the remaining units were classified as pINT (black dots). Blue dashed lines represent classification thresholds.

(B) Number of unresponsive (white) and responsive speed (blue) and non-speed (gray) cells among MEC populations of pINT (top) and pPC (bottom) following PPN stimulation. Numbers in the middle of the charts display total number of recorded cells. ***$p < 0.001$, two-proportions Z test between number of responsive pINT and pPC.

(C) Total number of responsive (blue) and unresponsive (white) pINT and pPC cells in the whole population of speed (left two bars) and non-speed (right two bars) cells recorded in MEC. Percentages above blue bars indicate proportion of responsive cells. **$p < 0.01$, ***$p < 0.001$, two-proportions Z test; n.s., not significant.

(D) Comparison of the number of responsive (blue) and unresponsive (white) cells for different functional populations in MEC. Percentages above blue bars indicate proportion of responsive cells in each functional cell class. *$p < 0.05$ and **$p < 0.01$, two-proportions Z test.

(E) Panels 1 and 3 from left: Circular plots displaying firing rate as a function of head direction (black line) for two representative head direction cells recorded in MEC during different screening sessions. Also represented are dwell times in each direction (blue inner line). Numbers indicate peak firing rate. Panels 2 and 4 from left: raster plots (top) and PSTH (bottom; bins, 1 ms) for the same head direction cells showing absolute changes in firing rate aligned to the onset of optogenetic laser pulses in PPN (blue shaded area) during stimulation sessions.

(F) Panels 1 and 3 from left: Path plot (gray line) with superimposed spiking activity (red dots) of two grid cells recorded in MEC during different screening sessions. Panels 2 and 4 from left: raster plots (top) and PSTH (bottom) for the same grid cells showing absolute changes in firing rate aligned to the onset of optogenetic laser pulses in PPN (blue window) during stimulation sessions (PSTH bins, 1 ms).

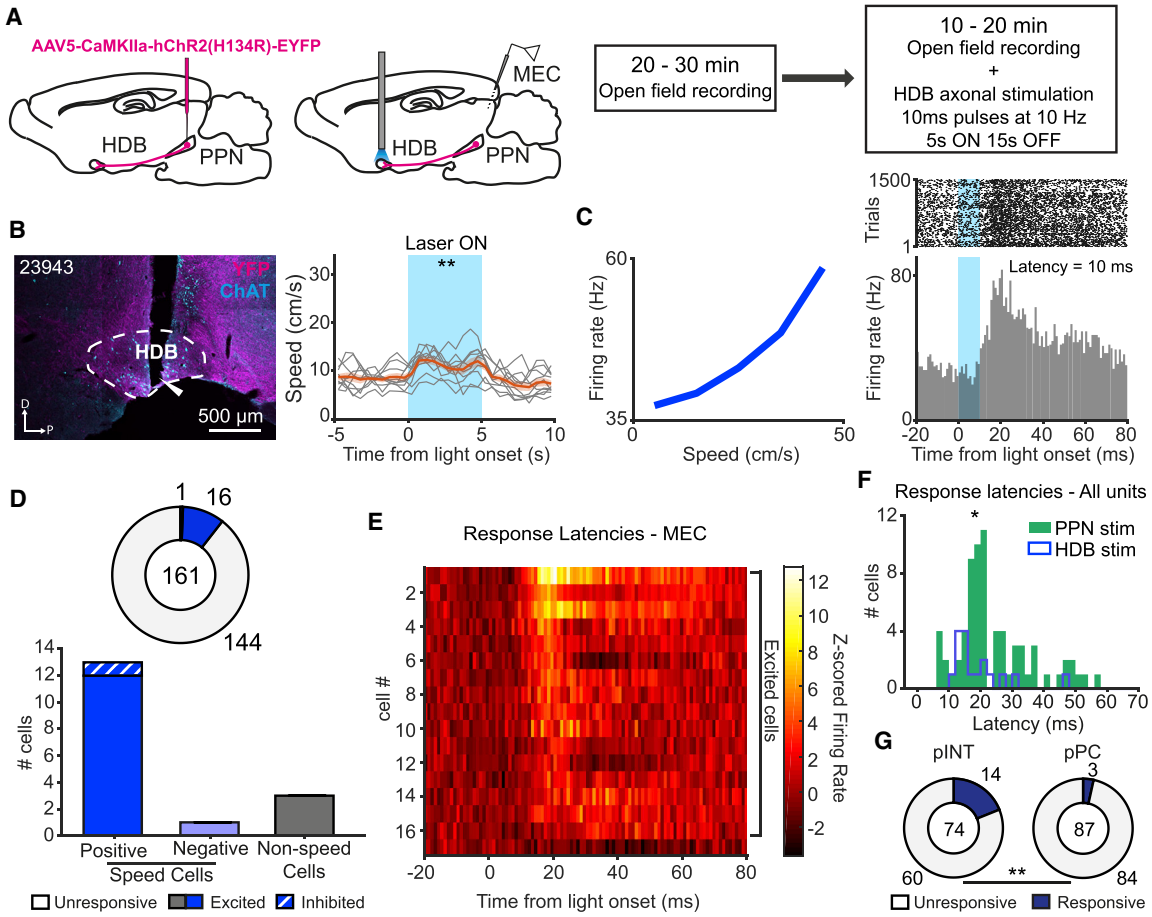

Figure 6. Cells in MEC Respond to Optogenetic Stimulation of PPN-Originating Axonal Inputs in HDB

(A) Implantation and recording procedures. Left: AAV5-CamKIIa-hChR2(H134R)-EYFP was injected in PPN (n = 5), followed by implantation of an optic fiber in HDB and tetrodes in MEC. Right: the recording protocol consisted of a baseline screening session in the open field, followed by a stimulation session, where laser stimulation was delivered to PPN terminals in HDB.

(B) Left: sagittal fluorescence photomicrograph of one rat (rat number shown in top left corner) showing ChR2 expression (magenta) and optic fiber placement in HDB. HDB anatomical border defined by ChAT immunofluorescence staining (cyan). White arrow indicates tip of the optic fiber. Scale bar: 500 µm. Right: average running speed during optogenetic stimulation of PPN axonal terminals in HDB (gray, ten individual sessions; orange, mean ± SEM of individual sessions). Note that changes in running speed induced by HDB stimulation were weaker than after direct PPN stimulation. **p < 0.01, Wilcoxon signed-rank test between pre-stimulation and stimulation epochs.

(C) Left: representative example of the speed tuning curve of a positive speed cell in MEC recorded during the baseline session. Right: raster plot (top) and PSTH (bottom; 1 ms bins) for the same cell displaying absolute changes in firing rate aligned to the onset of optogenetic stimulation in HDB (blue window).

(D) Top: proportion of unresponsive (white), excited (blue), and inhibited (dashed blue) cells recorded in MEC, following stimulation of PPN axons in HDB. Total number of recorded cells is displayed in the center. Bottom: summary of numbers of responsive speed cells (positive speed cells, left bar; negative speed cells, middle bar) and non-speed cells (right bar) in MEC, broken down by response type (excitation, filled bars; inhibition, dashed bars).

(E) Color-coded summary of changes in firing activity of all responsive cells recorded in MEC, sorted by response latency. *Z*-scored firing rates are color coded (scale bar).

(F) Histogram showing distribution of response latencies in all responsive MEC cells following stimulation of PPN axons in HDB (blue) or following somatic stimulation in PPN (green). *p < 0.01, Wilcoxon rank-sum test.

(G) Number of unresponsive (white) and responsive (blue) cells among MEC populations of pINT (top) and pPC (bottom) following stimulation of PPN axons in HDB. Numbers in the middle of the charts display total number of recorded cells. **p < 0.01, two-proportions *Z* test.

when MEC units were excited or inhibited by somatic PPN stimulation (HDB stimulation: n = 17, median latency = 15.0 ms; PPN stimulation: n = 71, median latency = 20.0 ms; $Z = 2.1$, p = 0.03, Wilcoxon rank-sum test; Figures 6E and 6F), further supporting the placement of HDB as an intermediate node between PPN and MEC and ruling out antidromic stimulation of PPN neurons as the source of MEC activation. Similar to the results with direct PPN stimulation, we observed responses in 14 of 74 (19.0%) pINT and in 3 of 87 pPC (5.7%) following stimulation of PPN axons in HDB ($Z = 3.2$, $p = 1.5 \times 10^{-3}$, two-proportions Z-test; Figure 6G), with 13 responsive pINT and one responsive pPC classified as speed cells ($Z = 2.5$, p = 0.014, two-proportions *Z* test). Also here we observed a greater number of responsive pINT than pPC in the entire population of speed cells (n = 55;

pPC, 1 of 16 [6.3%]; pINT, 13 of 39 [33.3%]; $Z = 2.1$, $p = 0.04$, two-proportions Z-test), but not in the entire population of non-speed cells (n = 106; pPC, 2 of 71 [2.8%]; pINT, 1 of 35 [2.9%]; $Z = 0$, $p = 0.99$, two-proportions Z test). We observed again that speed-modulated pINT were more responsive than non-speed-modulated pINT (speed-modulated pINT, 13 of 39 [33.3%]; non-speed-modulated pINT, 1 of 35 [2.9%]; $Z = 3.3$, $p = 8.4 \times 10^{-4}$, two-proportions Z test), a difference that was not observed for pPC (speed-modulated pPC, 1 of 16 [6.3%]; non-speed-modulated pPC, 2 of 71 [2.8%]; $Z = 0.7$, $p = 0.5$, two-proportions Z test). These results suggest once again that speed-modulated pINT in MEC are likely to be the main target of motor efferent inputs coming from PPN.

Finally, to further confirm the ability of HDB to drive changes in the activity of speed cells in MEC, we asked if a similar effect could be elicited by direct somatic stimulation of HDB neurons (Figure S6). In line with previous evidence showing post-synaptic responses in MEC following MSDB stimulation (Justus et al., 2017), optogenetic stimulation of local HDB neurons induced activity changes in MEC speed cells (positive speed cells: n = 2 excited, n = 2 inhibited) but also in additional MEC cell populations with no speed modulation (n = 7 excited, n = 11 inhibited) (Figures S6C and S6D). Compared with axonal stimulation of PPN terminals in HDB, somatic stimulation of HDB affected a more diverse population of MEC cells and was less restricted to speed-modulated neurons, possibly reflecting activation of a wider range of MEC afferents. Response latencies in MEC cells following HDB somatic stimulation were similar to latencies following stimulation of PPN axonal terminals in HDB (HDB axonal stimulation: n = 17, median latency 15 ms; HDB somatic stimulation: n = 22, median 16.5 ms; $Z = 0.6$, $p = 0.53$, Wilcoxon rank-sum test; Figures S6E and S6F). Collectively, the results suggest that HDB, under the control of direct projections from PPN, can mediate the effects of locomotor activation on speed cell activity in MEC.

DISCUSSION

In this study we provide anatomical and functional evidence for a circuit linking locomotor brainstem regions, via the HDB region in the basal forebrain, to the activity of speed cells in MEC. We show that locomotion speed is represented at each level of the pathway, with all levels—PPN, HDB, and MEC—displaying a sizable population of neurons with firing rates linearly tuned to the animal's running speed. Our results agree with previous studies identifying speed-modulated neurons in MEC (Sargolini et al., 2006; Kropff et al., 2015; Hinman et al., 2016; Ye et al., 2018) as well as MSDB (which the HDB is part of) (King et al., 1998; Zhou et al., 1999; Fuhrmann et al., 2015; Justus et al., 2017) and MLR (Lee et al., 2014; Roseberry et al., 2016; Caggiano et al., 2018). In the present work, we take these observations further by showing (1) that speed cells and other cells in HDB and MEC can be modulated by optogenetic stimulation in PPN; (2) that following stimulation of PPN cell bodies, average spike latencies in HDB are shorter than those in MEC; and (3) that modulation of MEC cells is similarly induced by stimulation of PPN axons at the level of HDB, with shorter response latencies than following somatic PPN stimulation. Taken together with our finding that axons of PPN cells terminate around HDB cells with projections to MEC, these observations point to the PPN-HDB-MEC circuit as a pathway for conveying locomotor information to dynamic spatial representations in MEC.

A large body of literature supports the role of PPN, and the wider region of the MLR, in the activation of locomotor programs (Skinner and Garcia-Rill, 1984; Garcia-Rill et al., 1987; Roseberry et al., 2016; Caggiano et al., 2018). Within the MLR, PPN appears to be particularly relevant for the implementation of exploratory locomotion (Caggiano et al., 2018). Glutamatergic neurons in the MLR have been shown to be tightly coupled to locomotor onset and to reliably represent the animal's running speed (Roseberry et al., 2016; Caggiano et al., 2018; Josset et al., 2018). A role in locomotion has also been demonstrated for the cholinergic neurons of the PPN (Roseberry et al., 2016; Xiao et al., 2016; Josset et al., 2018). Using our optogenetic approach, we activated a broad spectrum of PPN cells that engaged locomotion, but could, under some conditions, also promote transient immobility. This immobilization may be driven by putative ChR2-expressing GABA neurons, whose activation in PPN is known to halt locomotion (Roseberry et al., 2016). Alternatively, as onset and offset of locomotion were induced in different animals, with different stimulation sites, the behavioral outcome may depend on anatomically segregated subpopulations of glutamatergic neurons (Leiras et al., 2017, Society for Neuroscience Abstracts 232.08), in agreement with proposals that different anatomical and functional microcircuits within PPN are responsible for the implementation of different but competing motor programs (Leiras et al., 2017, Society for Neuroscience Abstracts 232.08; Martinez-Gonzalez et al., 2011; Mena-Segovia and Bolam, 2017; Josset et al., 2018). The behavioral outcome of PPN stimulation in the present study might be contingent on the position of the optic fiber with respect to these sub-circuits and might therefore reflect the extent of activation of one circuit instead of the other. In most cases, however, the stimulation likely activated outputs from both sub-circuits, discharging HDB and MEC neurons downstream to both circuits and implying that antagonistic PPN subpopulations may provide locomotor cues to overlapping downstream regions during active exploration. Unfortunately, with our current methods, it is not possible to dissect the exact functional and anatomical relationship between each recorded unit in HDB and MEC and the PPN sub-circuit that modulates their activity.

Brainstem locomotor information is likely distributed to a broad range of cortical and subcortical areas where they can function as motor efference copies (Holst and Mittelstaedt, 1950; Sperry, 1950; von Helmholtz, 1962). In this context, while speed cells that fire retrospectively to locomotion might reflect proprioceptive feedback, the prospective temporal biases we observed in subsets of speed cells along the entire PPN-HDB-MEC circuit may be part of a motor command chain sending ascending preparatory locomotor signals to widespread brain circuits prior to the implementation of motor programs or to kinetic changes in locomotion. Upon reaching their targets, these inputs could be used to generate a local speed code that continuously reflects ongoing locomotion and modulates neuronal function accordingly. In line with this notion, MLR projections to the basal forebrain have been shown to modulate neuronal

activity in the mouse primary visual cortex as a function of locomotor state (Lee et al., 2014). Further supporting the existence of a wide cortical distribution of motor efference copies or motor command signals, changes in neuronal firing rates as a function of movement or running speed have been reported in a number of primary sensory cortices, including visual (Niell and Stryker, 2010; Lee et al., 2014; Dipoppa et al., 2018), somatosensory (Ayaz et al., 2019), and auditory (Schneider et al., 2014, 2018) cortices.

Our results point to the HDB, and more broadly the MSDB, as an intermediate node in a pathway transmitting locomotor speed information from the brainstem to the navigational systems of the entorhinal cortex. The observations further show that specific stimulation of projections from PPN to HDB can elicit movement. The locomotion-inducing effects of PPN terminal stimulation in HDB were smaller than after direct PPN stimulation, possibly because direct somatic PPN stimulation not only targets ascending projections to MSDB, including HDB, but also basal ganglia circuits and descending projections to medulla and spinal cord targets (Martinez-Gonzalez et al., 2011; Mena-Segovia and Bolam, 2017). Alternatively, or additionally, PPN terminal stimulation in HDB might reach the same targets through antidromic activation but with less efficiency because the number of activated PPN cells would be a lot smaller. Antidromic activation cannot, however, account for the shorter MEC response latencies observed after axonal stimulation in HDB than after somatic PPN stimulation. The observation of downstream neuronal responses in MEC after PPN and HDB stimulation is consistent with a study showing monosynaptic responses in MEC cells following stimulation of projections from populations of speed-modulated glutamatergic MSDB cells (Justus et al., 2017). At first glance, these findings seem at odds with observations showing spared speed modulation of MEC cells after pharmacological or optogenetic inhibition of cell populations in MSDB (Hinman et al., 2016; Dannenberg et al., 2019); however, because, in these studies, the infusion cannula and the optic fiber were implanted at the dorsal pole of MSDB complex, these observations may not rule out residual activity in ventrally located HDB cells as a possible source of speed coding in MEC. The interdependence between locomotor circuits in PPN and speed cell activity in HDB and MEC, demonstrated in this study, thus identify the HDB region of MSDB as a relay area between locomotor circuits in PPN and position-coding systems in MEC.

Our findings further show that in MEC, the targeting of ascending speed signals from PPN and HDB is not uniformly distributed across cell types but preferentially modulates the activity of speed cells more than other functional cell classes. The majority of the responsive entorhinal speed cells had characteristics reminiscent of interneurons (Ye et al., 2018). MEC interneurons form dense recurrent inhibitory networks that may orchestrate the spatial periodicity of grid cells, as well as the spatial firing properties of other MEC neurons (Bonnevie et al., 2013; Couey et al., 2013; Buetfering et al., 2014). PV-expressing interneurons have been shown to be particularly essential for accurate encoding of locomotion speed (Miao et al., 2017), as well as for the stability of spatial firing properties in grid cells (Buetfering et al., 2014; Miao et al., 2017). By showing here that PPN stimulation preferentially targets speed-modulated MEC interneurons, we speculate that ascending motor signals from the brainstem spread widely through local MEC interneuron networks, which might then gate the integration of speed signals by other functional cell types required for spatial representations. This possibility could help explain why functional cell types such as grid cells, whose activity depends on active locomotor cues (Winter et al., 2015b), showed considerably lower responsivity to PPN stimulation than speed cells. Within MEC, locomotor inputs need to be integrated with other self-motion cues, such as visual information, optic flow, and vestibular signals (Jacob et al., 2014; Pérez-Escobar et al., 2016; Campbell and Giocomo, 2018; Campbell et al., 2018), but also with head direction signals, that contribute to grid cell firing (Sargolini et al., 2006; Winter et al., 2015a). Along with other movement-correlated signals (Raudies et al., 2015), the combination of these inputs may be required for the dynamic representation of position that underlies path integration (Fuhs and Touretzky, 2006; McNaughton et al., 2006; Burgess et al., 2007; Hasselmo et al., 2007; Burak and Fiete, 2009). Moreover, because some collaterals of fast-spiking GABAergic speed cells in MEC may reach the hippocampus (Melzer et al., 2012; Ye et al., 2018), it is conceivable that locomotor inputs from PPN may also play a role in synchronization of activity in MEC and hippocampus, possibly in combination with septohippocampal and other septoentorhinal speed inputs (Fuhrmann et al., 2015; Justus et al., 2017).

The PPN-HDB-MEC circuit described here most likely represents only one of several possible pathways by which locomotor signals can reach MEC. Our tetrode recordings reveal the presence of speed-modulated neurons in the vicinity of, but outside, the PPN, HDB, and MEC, with subtle regional differences in population number and strength of speed modulation. This indicates that speed-related information is not limited to the PPN-HDB-MEC circuit here described. Additionally, our anatomy results show an appreciable co-occurrence of PPN efferents and MEC-projecting neurons not only in HDB but also in the SuM and the Re, areas that also elicit locomotion when electrically stimulated (Sinnamon, 1984) and that play a role in spatial learning and navigation (Shahidi et al., 2004; Ito et al., 2015). Therefore, these areas might play a complementary role in relaying speed information from PPN to MEC. However, it is yet unclear whether the apparently ubiquitous nature of speed coding in the brain consists of multiple systems for representation of locomotor activity, with different brain regions relying on different sources of locomotor signals or, alternatively, whether speed coding in different systems is all inherited from a single source such as the MLR.

In sum, this study supports the existence of a speed-encoding neuronal circuit that connects PPN to MEC, via HDB, and that is functionally linked to the activity of downstream speed cells in MEC. Our results indicate that ascending projections from PPN provide a possible source of information about ongoing locomotor activity emerging during exploratory behavior, which could provide the type of moment-by-moment update of the animal's displacement that is required to instruct the activity of spatially tuned cell types in MEC, such as grid cells, during navigation.

STAR★METHODS

Detailed methods are provided in the online version of this paper and include the following:

- KEY RESOURCES TABLE
- RESOURCE AVAILABILITY
  - Lead Contact
  - Materials Availability
  - Data and Code Availability
- EXPERIMENTAL MODEL AND SUBJECT DETAILS
- METHOD DETAILS
  - *In vivo* surgery
  - Tracer injections
  - Tetrode implants
  - Single unit recordings
  - Spike sorting
  - Optogenetic stimulation
  - Laser-response analysis
  - Speed modulation
  - Distinction between putative principal cells and interneurons
  - Spatial tuning curves
  - Grid score
  - Head direction score
  - Border score
  - Shuffling of spike data
  - Histological procedure for determining tetrode recording sites
  - Reconstruction of tetrode recording sites
  - Immunohistochemistry and imaging
- QUANTIFICATION AND STATISTICAL ANALYSIS

SUPPLEMENTAL INFORMATION

Supplemental Information can be found online at https://doi.org/10.1016/j.celrep.2020.108123.

ACKNOWLEDGMENTS

We thank G. Olsen for assistance with tracer injections; V. Frolov for help with programming; and H. Waade, K. Jenssen, A. M. Amundsgård, and K. Haugen for technical assistance in the recording experiments. This work was supported by two Advanced Investigator Grants from the European Research Council (GRIDCODE, 338865; ENSEMBLE, 268598), the Centre of Excellence Scheme and the National Infrastructure Scheme of the Research Council of Norway (Centre for Neural Computation, 223262; NORBRAIN1, 197467), and the Kavli Foundation.

AUTHOR CONTRIBUTIONS

M.M.C., N.T., M.-B.M., and E.I.M. conceptualized the project and designed experiments. M.M.C. and N.T. performed all experiments, data collection, and analyses; E.K. designed speed cell analyses. M.P.W. helped design and analyze anatomy experiments. M.M.C., N.T., M.-B.M., and E.I.M. wrote the paper with input from all authors.

DECLARATION OF INTERESTS

The authors declare no competing interests.

Received: March 9, 2020
Revised: May 26, 2020
Accepted: August 18, 2020
Published: September 8, 2020

REFERENCES

Amaral, D.G., and Kurz, J. (1985). An analysis of the origins of the cholinergic and noncholinergic septal projections to the hippocampal formation of the rat. J. Comp. Neurol. *240*, 37–59.

Ayaz, A., Stäuble, A., Hamada, M., Wulf, M.A., Saleem, A.B., and Helmchen, F. (2019). Layer-specific integration of locomotion and sensory information in mouse barrel cortex. Nat. Commun. *10*, 2585.

Bonnevie, T., Dunn, B., Fyhn, M., Hafting, T., Derdikman, D., Kubie, J.L., Roudi, Y., Moser, E.I., and Moser, M.B. (2013). Grid cells require excitatory drive from the hippocampus. Nat. Neurosci. *16*, 309–317.

Brandon, M.P., Bogaard, A.R., Libby, C.P., Connerney, M.A., Gupta, K., and Hasselmo, M.E. (2011). Reduction of theta rhythm dissociates grid cell spatial periodicity from directional tuning. Science *332*, 595–599.

Buetfering, C., Allen, K., and Monyer, H. (2014). Parvalbumin interneurons provide grid cell-driven recurrent inhibition in the medial entorhinal cortex. Nat. Neurosci. *17*, 710–718.

Burak, Y., and Fiete, I.R. (2009). Accurate path integration in continuous attractor network models of grid cells. PLoS Comput. Biol. *5*, e1000291.

Burgess, N., Barry, C., and O'Keefe, J. (2007). An oscillatory interference model of grid cell firing. Hippocampus *17*, 801–812.

Buzsáki, G. (2002). Theta oscillations in the hippocampus. Neuron *33*, 325–340.

Caggiano, V., Leiras, R., Goñi-Erro, H., Masini, D., Bellardita, C., Bouvier, J., Caldeira, V., Fisone, G., and Kiehn, O. (2018). Midbrain circuits that set locomotor speed and gait selection. Nature *553*, 455–460.

Campbell, M.G., and Giocomo, L.M. (2018). Self-motion processing in visual and entorhinal cortices: inputs, integration, and implications for position coding. J. Neurophysiol. *120*, 2091–2106.

Campbell, M.G., Ocko, S.A., Mallory, C.S., Low, I.I.C., Ganguli, S., and Giocomo, L.M. (2018). Principles governing the integration of landmark and self-motion cues in entorhinal cortical codes for navigation. Nat. Neurosci. *21*, 1096–1106.

Chen, G., King, J.A., Burgess, N., and O'Keefe, J. (2013). How vision and movement combine in the hippocampal place code. Proc. Natl. Acad. Sci. U S A *110*, 378–383.

Colgin, L.L. (2016). Rhythms of the hippocampal network. Nat. Rev. Neurosci. *17*, 239–249.

Couey, J.J., Witoelar, A., Zhang, S.J., Zheng, K., Ye, J., Dunn, B., Czajkowski, R., Moser, M.B., Moser, E.I., Roudi, Y., and Witter, M.P. (2013). Recurrent inhibitory circuitry as a mechanism for grid formation. Nat. Neurosci. *16*, 318–324.

Czurkó, A., Hirase, H., Csicsvari, J., and Buzsáki, G. (1999). Sustained activation of hippocampal pyramidal cells by 'space clamping' in a running wheel. Eur. J. Neurosci. *11*, 344–352.

Dannenberg, H., Kelley, C., Hoyland, A., Monaghan, C.K., and Hasselmo, M.E. (2019). The firing rate speed code of entorhinal speed cells differs across behaviorally relevant time scales and does not depend on medial septum inputs. J. Neurosci. *39*, 3434–3453.

Dipoppa, M., Ranson, A., Krumin, M., Pachitariu, M., Carandini, M., and Harris, K.D. (2018). Vision and locomotion shape the interactions between neuron types in mouse visual cortex. Neuron *98*, 602–615.e8.

Etienne, A.S., and Jeffery, K.J. (2004). Path integration in mammals. Hippocampus *14*, 180–192.

Frank, L.M., Brown, E.N., and Wilson, M.A. (2001). A comparison of the firing properties of putative excitatory and inhibitory neurons from CA1 and the entorhinal cortex. J. Neurophysiol. *86*, 2029–2040.

Fuchs, E.C., Neitz, A., Pinna, R., Melzer, S., Caputi, A., and Monyer, H. (2016). Local and distant input controlling excitation in layer II of the medial entorhinal cortex. Neuron *89*, 194–208.

Fuhrmann, F., Justus, D., Sosulina, L., Kaneko, H., Beutel, T., Friedrichs, D., Schoch, S., Schwarz, M.K., Fuhrmann, M., and Remy, S. (2015). Locomotion, theta oscillations, and the speed-correlated firing of hippocampal neurons are controlled by a medial septal glutamatergic circuit. Neuron *86*, 1253–1264.

Fuhs, M.C., and Touretzky, D.S. (2006). A spin glass model of path integration in rat medial entorhinal cortex. J. Neurosci. *26*, 4266–4276.

Fyhn, M., Molden, S., Witter, M.P., Moser, E.I., and Moser, M.B. (2004). Spatial representation in the entorhinal cortex. Science *305*, 1258–1264.

Fyhn, M., Hafting, T., Treves, A., Moser, M.B., and Moser, E.I. (2007). Hippocampal remapping and grid realignment in entorhinal cortex. Nature *446*, 190–194.

Gallistel, C.R. (1990). The Organization of Learning (Bradford Books/MIT Press).

Garcia-Rill, E., Houser, C.R., Skinner, R.D., Smith, W., and Woodward, D.J. (1987). Locomotion-inducing sites in the vicinity of the pedunculopontine nucleus. Brain Res. Bull. *18*, 731–738.

Gaykema, R.P., Luiten, P.G., Nyakas, C., and Traber, J. (1990). Cortical projection patterns of the medial septum-diagonal band complex. J. Comp. Neurol. *293*, 103–124.

Giocomo, L.M., Stensola, T., Bonnevie, T., Van Cauter, T., Moser, M.B., and Moser, E.I. (2014). Topography of head direction cells in medial entorhinal cortex. Curr. Biol. *24*, 252–262.

Gothard, K.M., Skaggs, W.E., and McNaughton, B.L. (1996). Dynamics of mismatch correction in the hippocampal ensemble code for space: interaction between path integration and environmental cues. J. Neurosci. *16*, 8027–8040.

Hafting, T., Fyhn, M., Molden, S., Moser, M.B., and Moser, E.I. (2005). Microstructure of a spatial map in the entorhinal cortex. Nature *436*, 801–806.

Hallanger, A.E., and Wainer, B.H. (1988). Ascending projections from the pedunculopontine tegmental nucleus and the adjacent mesopontine tegmentum in the rat. J. Comp. Neurol. *274*, 483–515.

Hardcastle, K., Maheswaranathan, N., Ganguli, S., and Giocomo, L.M. (2017). A multiplexed, heterogeneous, and adaptive code for navigation in medial entorhinal cortex. Neuron *94*, 375–387.e7.

Hasselmo, M.E., Giocomo, L.M., and Zilli, E.A. (2007). Grid cell firing may arise from interference of theta frequency membrane potential oscillations in single neurons. Hippocampus *17*, 1252–1271.

Hinman, J.R., Brandon, M.P., Climer, J.R., Chapman, G.W., and Hasselmo, M.E. (2016). Multiple Running Speed Signals in Medial Entorhinal Cortex. Neuron *91*, 666–679.

Holst, E.v., and Mittelstaedt, H. (1950). Das Reafferencprinczip. Naturwissenschaften *37*, 464–476.

Ito, H.T., Zhang, S.J., Witter, M.P., Moser, E.I., and Moser, M.B. (2015). A prefrontal-thalamo-hippocampal circuit for goal-directed spatial navigation. Nature *522*, 50–55.

Jacob, P.Y., Poucet, B., Liberge, M., Save, E., and Sargolini, F. (2014). Vestibular control of entorhinal cortex activity in spatial navigation. Front. Integr. Nuerosci. *8*, 38.

Jacob, P.Y., Gordillo-Salas, M., Facchini, J., Poucet, B., Save, E., and Sargolini, F. (2017). Medial entorhinal cortex and medial septum contribute to self-motion-based linear distance estimation. Brain Struct. Funct. *222*, 2727–2742.

Josset, N., Roussel, M., Lemieux, M., Lafrance-Zoubga, D., Rastqar, A., and Bretzner, F. (2018). Distinct contributions of mesencephalic locomotor region nuclei to locomotor control in the freely behaving mouse. Curr. Biol. *28*, 884–901.e3.

Justus, D., Dalügge, D., Bothe, S., Fuhrmann, F., Hannes, C., Kaneko, H., Friedrichs, D., Sosulina, L., Schwarz, I., Elliott, D.A., et al. (2017). Glutamatergic synaptic integration of locomotion speed via septoentorhinal projections. Nat. Neurosci. *20*, 16–19.

King, C., Recce, M., and O'Keefe, J. (1998). The rhythmicity of cells of the medial septum/diagonal band of Broca in the awake freely moving rat: relationships with behaviour and hippocampal theta. Eur. J. Neurosci. *10*, 464–477.

Koenig, J., Linder, A.N., Leutgeb, J.K., and Leutgeb, S. (2011). The spatial periodicity of grid cells is not sustained during reduced theta oscillations. Science *332*, 592–595.

Kropff, E., Carmichael, J.E., Moser, M.B., and Moser, E.I. (2015). Speed cells in the medial entorhinal cortex. Nature *523*, 419–424.

Langston, R.F., Ainge, J.A., Couey, J.J., Canto, C.B., Bjerknes, T.L., Witter, M.P., Moser, E.I., and Moser, M.B. (2010). Development of the spatial representation system in the rat. Science *328*, 1576–1580.

Lee, A.M., Hoy, J.L., Bonci, A., Wilbrecht, L., Stryker, M.P., and Niell, C.M. (2014). Identification of a brainstem circuit regulating visual cortical state in parallel with locomotion. Neuron *83*, 455–466.

Losier, B.J., and Semba, K. (1993). Dual projections of single cholinergic and aminergic brainstem neurons to the thalamus and basal forebrain in the rat. Brain Res. *604*, 41–52.

Martin, M.M., Horn, K.L., Kusman, K.J., and Wallace, D.G. (2007). Medial septum lesions disrupt exploratory trip organization: evidence for septohippocampal involvement in dead reckoning. Physiol. Behav. *90*, 412–424.

Martinez-Gonzalez, C., Bolam, J.P., and Mena-Segovia, J. (2011). Topographical organization of the pedunculopontine nucleus. Front. Neuroanat. *5*, 22.

McNaughton, B.L., Barnes, C.A., and O'Keefe, J. (1983). The contributions of position, direction, and velocity to single unit activity in the hippocampus of freely-moving rats. Exp. Brain Res. *52*, 41–49.

McNaughton, B.L., Barnes, C.A., Gerrard, J.L., Gothard, K., Jung, M.W., Knierim, J.J., Kudrimoti, H., Qin, Y., Skaggs, W.E., Suster, M., and Weaver, K.L. (1996). Deciphering the hippocampal polyglot: the hippocampus as a path integration system. J. Exp. Biol. *199*, 173–185.

McNaughton, B.L., Battaglia, F.P., Jensen, O., Moser, E.I., and Moser, M.B. (2006). Path integration and the neural basis of the 'cognitive map'. Nat. Rev. Neurosci. *7*, 663–678.

Melzer, S., Michael, M., Caputi, A., Eliava, M., Fuchs, E.C., Whittington, M.A., and Monyer, H. (2012). Long-range-projecting GABAergic neurons modulate inhibition in hippocampus and entorhinal cortex. Science *335*, 1506–1510.

Mena-Segovia, J., and Bolam, J.P. (2017). Rethinking the pedunculopontine nucleus: from cellular organization to function. Neuron *94*, 7–18.

Miao, C., Cao, Q., Moser, M.B., and Moser, E.I. (2017). Parvalbumin and somatostatin interneurons control different space-coding networks in the medial entorhinal cortex. Cell *171*, 507–521.e17.

Mittelstaedt, M.L., and Mittelstaedt, H. (1980). Homing by path integration in a mammal. Naturwissenschaften *67*, 566–567.

Moser, E.I., Roudi, Y., Witter, M.P., Kentros, C., Bonhoeffer, T., and Moser, M.B. (2014). Grid cells and cortical representation. Nat. Rev. Neurosci. *15*, 466–481.

Niell, C.M., and Stryker, M.P. (2010). Modulation of visual responses by behavioral state in mouse visual cortex. Neuron *65*, 472–479.

Paxinos, G., and Watson, C. (2007). The Rat Brain in Stereotaxic Coordinates, 6th (Academic Press/Elsevier).

Pérez-Escobar, J.A., Kornienko, O., Latuske, P., Kohler, L., and Allen, K. (2016). Visual landmarks sharpen grid cell metric and confer context specificity to neurons of the medial entorhinal cortex. eLife *5*, e16937.

Raudies, F., Brandon, M.P., Chapman, G.W., and Hasselmo, M.E. (2015). Head direction is coded more strongly than movement direction in a population of entorhinal neurons. Brain Research *1621*, 355–367.

Ravassard, P., Kees, A., Willers, B., Ho, D., Aharoni, D.A., Cushman, J., Aghajan, Z.M., and Mehta, M.R. (2013). Multisensory control of hippocampal spatiotemporal selectivity. Science *340*, 1342–1346.

Redish, A.D., Rosenzweig, E.S., Bohanick, J.D., McNaughton, B.L., and Barnes, C.A. (2000). Dynamics of hippocampal ensemble activity realignment: time versus space. J. Neurosci. *20*, 9298–9309.

Roseberry, T.K., Lee, A.M., Lalive, A.L., Wilbrecht, L., Bonci, A., and Kreitzer, A.C. (2016). Cell-type-specific control of brainstem locomotor circuits by basal ganglia. Cell *164*, 526–537.

Rowland, D.C., Obenhaus, H.A., Skytøen, E.R., Zhang, Q., Kentros, C.G., Moser, E.I., and Moser, M.B. (2018). Functional properties of stellate cells in medial entorhinal cortex layer II. eLife *7*, e36664.

Ryczko, D., and Dubuc, R. (2013). The multifunctional mesencephalic locomotor region. Curr. Pharm. Des. *19*, 4448–4470.

Sargolini, F., Fyhn, M., Hafting, T., McNaughton, B.L., Witter, M.P., Moser, M.B., and Moser, E.I. (2006). Conjunctive representation of position, direction, and velocity in entorhinal cortex. Science *312*, 758–762.

Schneider, D.M., Nelson, A., and Mooney, R. (2014). A synaptic and circuit basis for corollary discharge in the auditory cortex. Nature *513*, 189–194.

Schneider, D.M., Sundararajan, J., and Mooney, R. (2018). A cortical filter that learns to suppress the acoustic consequences of movement. Nature *561*, 391–395.

Shahidi, S., Motamedi, F., and Naghdi, N. (2004). Effect of reversible inactivation of the supramammillary nucleus on spatial learning and memory in rats. Brain Res. *1026*, 267–274.

Shik, M.L., Severin, F.V., and Orlovsky, G.N. (1969). Control of walking and running by means of electrical stimulation of the mesencephalon. Electroencephalogr. Clin. Neurophysiol. *26*, 549.

Sinnamon, H.M. (1984). Forelimb and hindlimb stepping by the anesthetized rat elicited by electrical stimulation of the diencephalon and mesencephalon. Physiol. Behav. *33*, 191–199.

Skinner, R.D., and Garcia-Rill, E. (1984). The mesencephalic locomotor region (MLR) in the rat. Brain Res. *323*, 385–389.

Solstad, T., Boccara, C.N., Kropff, E., Moser, M.B., and Moser, E.I. (2008). Representation of geometric borders in the entorhinal cortex. Science *322*, 1865–1868.

Sperry, R.W. (1950). Neural basis of the spontaneous optokinetic response produced by visual inversion. J. Comp. Physiol. Psychol. *43*, 482–489.

Tago, H., Kimura, H., and Maeda, T. (1986). Visualization of detailed acetylcholinesterase fiber and neuron staining in rat brain by a sensitive histochemical procedure. J. Histochem. Cytochem. *34*, 1431–1438.

Tanke, N., Borst, J.G.G., and Houweling, A.R. (2018). Single-cell stimulation in barrel cortex influences psychophysical detection performance. J. Neurosci. *38*, 2057–2068.

Terrazas, A., Krause, M., Lipa, P., Gothard, K.M., Barnes, C.A., and McNaughton, B.L. (2005). Self-motion and the hippocampal spatial metric. J. Neurosci. *25*, 8085–8096.

Unal, G., Joshi, A., Viney, T.J., Kis, V., and Somogyi, P. (2015). Synaptic targets of medial septal projections in the hippocampus and extrahippocampal cortices of the mouse. J. Neurosci. *35*, 15812–15826.

von Helmholtz, H. (1962). Treatise on Physiological Optics*Vol. 3* (Dover).

Wiener, S.I., Paul, C.A., and Eichenbaum, H. (1989). Spatial and behavioral correlates of hippocampal neuronal activity. J. Neurosci. *9*, 2737–2763.

Winter, S.S., Clark, B.J., and Taube, J.S. (2015a). Spatial navigation. Disruption of the head direction cell network impairs the parahippocampal grid cell signal. Science *347*, 870–874.

Winter, S.S., Mehlman, M.L., Clark, B.J., and Taube, J.S. (2015b). Passive transport disrupts grid signals in the parahippocampal cortex. Curr. Biol. *25*, 2493–2502.

Woolf, N.J., and Butcher, L.L. (1986). Cholinergic systems in the rat brain: III. Projections from the pontomesencephalic tegmentum to the thalamus, tectum, basal ganglia, and basal forebrain. Brain Res. Bull. *16*, 603–637.

Xiao, C., Cho, J.R., Zhou, C., Treweek, J.B., Chan, K., McKinney, S.L., Yang, B., and Gradinaru, V. (2016). Cholinergic mesopontine signals govern locomotion and reward through dissociable midbrain pathways. Neuron *90*, 333–347.

Ye, J., Witter, M.P., Moser, M.B., and Moser, E.I. (2018). Entorhinal fast-spiking speed cells project to the hippocampus. Proc. Natl. Acad. Sci. U S A *115*, E1627–E1636.

Yoon, K., Buice, M.A., Barry, C., Hayman, R., Burgess, N., and Fiete, I.R. (2013). Specific evidence of low-dimensional continuous attractor dynamics in grid cells. Nat. Neurosci. *16*, 1077–1084.

Zhou, T.L., Tamura, R., Kuriwaki, J., and Ono, T. (1999). Comparison of medial and lateral septal neuron activity during performance of spatial tasks in rats. Hippocampus *9*, 220–234.

STAR★METHODS

KEY RESOURCES TABLE

REAGENT or RESOURCE	SOURCE	IDENTIFIER
Antibodies		
Streptavidin-Alexa Fluor 546	ThermoFisher Scientific	S11225
Fluorescent Nissl deep red 640/660	ThermoFisher Scientific	N-21483
Rabbit anti-GFP	ThermoFisher Scientific	A11122; RRID: AB_221569
Goat anti-ChAT	Merck Millipore	AB144P; RRID: AB_2079751
Donkey anti-rabbit Alexa Fluor 488	ThermoFisher Scientific	A21206; RRID: AB_2535792
Donkey anti-goat Alexa Fluor 568	ThermoFisher Scientific	A11057; RRID: AB_2534104
Donkey anti-goat Alexa Fluor 647	ThermoFisher Scientific	A21447; RRID: AB_2535864
Bacterial and Virus Strains		
AAV5-CaMKIIa-hChR2(H134R)-EYFP	UNC vector Core	Deisseroth stock
AAV5-CaMKIIa-EYFP	UNC vector Core	Deisseroth stock
Chemicals, Peptides, and Recombinant Proteins		
Biotinylated dextran amine (BDA)	Invitrogen	#D1956
Fast Blue	EMS Chemie	#9000002
ProLong diamond antifade mounting medium	ThermoFisher Scientific	P36965
OptiBond dental bonding agent	Kerr	Cat#33381
Charisma® dental filling composite	Kulzer	Cat# 66000098
Experimental Models: Organisms/Strains		
Rat: Long-Evans		N/A
Software and Algorithms		
DacqUSB	Axona Ltd.	http://www.axona.com/
Tint	Axona Ltd.	http://www.axona.com/
MATLAB R2019b	Mathworks	https://se.mathworks.com/
MClust 4.4	A.D. Redish	http://redishlab.neuroscience.umn.edu/MClust/MClust.html
Arduino UNO	Arduino	https://www.arduino.cc/
Zen (Blue Edition)	Zeiss	https://www.zeiss.com/microscopy/int/products/microscope-software/zen.html
Other		
Borosilicate glass pipettes for BDA injection	Harvard Apparatus	N/A
Controller for BDA injection	Stoelting	51595
30G syringe for FB injection	Hamilton	Neuros 75, 5 μl
Motorized pump connected to a microinjection digital controller for FB injection	World Precision Instruments	UMP3 and SYS-Micro4
Microdrive	Axona Ltd.	N/A
Polyimide-coated platinum-iridium (90-10%) wires	California Fine wire	N/A
Borosilicate glass pipettes for virus injection	World Precision Instruments	N/A
Motorized microinjection controller for virus injection	World Precision Instruments	Nanoliter 2010
Fiber-optic canula	Doric Lenses	250 μm diameter, MFC_200/245-0.53_11mm_ZF2.5(G)_FLT
Mono-fiber-optic patch cord	Doric Lenses	MFP_200/230/3000-0.48_8m_SMA_ZF2.5(F)

(*Continued on next page*)

Continued

REAGENT or RESOURCE	SOURCE	IDENTIFIER
473 nm laser	Shanghai Laser & Optics Co.	N/A
Mechanical shutter	Vincent Associates	LS3S2T1 Uniblitz shutter system
LSM 880 AxioImager Z2	Zeiss	N/A
Axio Scan.Z1	Zeiss	N/A

RESOURCE AVAILABILITY

Lead Contact

Further information and requests for resources and reagents should be directed to and will be fulfilled by the lead contact, Edvard I. Moser (edvard.moser@ntnu.no).

Materials Availability

This study did not generate new unique reagents.

Data and Code Availability

The datasets and code supporting the current study can be made available from the corresponding author on request.

EXPERIMENTAL MODEL AND SUBJECT DETAILS

Fifty-one wild-type Long-Evans rats (45 male, 6 female; aged 3-6 months; 300-700 g at implantation and/or virus/tracer injection) were bred in-house. They were initially housed in pairs in transparent cages (54 × 44 × 35 cm) and kept on a 12-h light-dark schedule, with food and water *ad libitum*. No previous procedures were conducted on the rats before the start of our experiments. Five of the rats (1 male, 4 female) were used for tracer injections. Twenty-four of the rats (22 male, 2 female) were implanted with tetrodes for extracellular single unit recordings. The remaining 22 rats (all male) were used for optogenetic manipulation experiments and were injected with either a channelrhodopsin-2-expressing virus (n = 18) or a control virus (n = 4), followed by optic fiber and tetrode implants. All experimental subjects used for single unit recordings and optogenetic manipulations were housed individually after surgery, and, following a 1-week recovery period, placed in a food restriction regime, with weight monitored daily and kept above 90% of pre-operative values. Experimental procedures were always performed during the dark phase of the light-dark cycle. Experiments were performed in compliance with the Norwegian Animal Welfare Act and the European Convention for the protection of Vertebrate Animals used for Experimental and Other Scientific Purposes.

METHOD DETAILS

In vivo surgery

All surgeries were performed under isoflurane anesthesia (airflow: 1 L/min, 5% isoflurane for induction and 1.0%–2.5% during surgery, adjusted by monitoring breathing and reflexes). The rats were initially placed in an induction plexiglass box filled with isoflurane vapor and then transferred to a stereotactic frame equipped with a nose mask connected to the isoflurane pump. At the beginning of the surgery, subcutaneous injections of buprenorphine (0.01-0.05 mg/Kg) and meloxicam (1 mg/Kg) were administered to provide additional analgesia, and atropine (0.05 mg/Kg) was injected subcutaneously to reduce respiratory tract secretions during the procedure. During surgery, body temperature was maintained by a heating pad set to 37°C, and subcutaneous fluid therapy was administered (0.9% saline, 3 ml/2h, 25 mL max). Before incision, we injected bupivacaine (1 mg/kg) subcutaneously, after which the skull was exposed and levelled by setting the same dorso-ventral coordinate at both bregma and lambda. Using a motorized drill, a small portion of the skull was thinned at the sagittal suture, to partially visualize the sagittal sinus. All tracer and virus injections, as well as tetrode and optic-fiber implants, were performed unilaterally, with medio-lateral (ML) coordinates measured relative to the middle of the sagittal sinus. To expose the surface of the brain above each area targeted for tracer and virus injections and tetrode/optic-fiber implants, a craniotomy was manually drilled at intended medio-lateral coordinates. Coordinates for PPN injections and implants were: 1.7-1.95 mm ML, and 0.80-1.80 mm anterior to the border of the transverse sinus, which was exposed at that ML coordinate. Coordinates for HDB injections and implants were: 0.7-1.2 mm ML, and 0.4-0.9 mm, anterior to bregma. Coordinates for MEC injections and implants were: 4.4-5.3 mm ML, and 0.15-0.30 mm anterior to border of the transverse sinus, exposed at that ML coordinate. For post-operative care, animals were subcutaneously injected with buprenorphine (0.01-0.05 mg/Kg), 8-12 hours post-surgery, and given oral meloxicam (1 mg/Kg), 24- and 48-hours post-surgery. The animals recovered from surgery for a minimum of 3 days before continuing with behavioral tasks.

Tracer injections

Classical neuronal tracers were used to map anatomical connections between PPN and MEC. Four animals were unilaterally injected with an anterograde tracer, biotinylated dextran amine (BDA, 10 kDa, 5% solution in 0.125 M phosphate buffer) in PPN, and a retrograde tracer, Fast Blue (FB, 2% solution in 0.9% saline), in MEC. We performed iontophoretic BDA injections in PPN with pulled borosilicate glass pipettes (20-30 μm tip diameter; Harvard Apparatus), using a controller (51595; Stoelting) that delivered an alternating current of 6 μA for 15-20 minutes (6 s on/off) at three adjacent anterior-posterior locations (coordinate range described above, minimum of 300 μm between injection sites), 5.2-7.0 mm ventral from the brain surface. In MEC, 150-250 nL of FB was injected at one or two locations 2.6-3.8 mm ventral from brain surface, using a 30G syringe (Neuros 75 5 μL, Hamilton) controlled by a motorized pump connected to a microinjection digital controller (UMP3 and SYS-Micro4, World Precision Instruments). The syringe was angled 20°, with the tip pointing forward, and with the injection rate set at 50 nL/min. After each injection the needle was left in place for 10 additional minutes to allow diffusion. To confirm HDB as a possible intermediate node of a circuit connecting PPN to MEC, one additional animal received a FB injection in HDB. This injection was performed the same way as injections in MEC, but 7.4 mm ventral to the surface of the brain and with 0° deviation from vertical. All animals used in tracer experiments were euthanized and perfused 7-10 days after tracer injections.

Tetrode implants

Tetrode microdrives were constructed by mounting four twisted 17 μm polyimide-coated platinum-iridium (90%–10%) wires (California Fine Wire) into microdrives with a single turning screw (Axona Ldt.). Electrode tips were plated with platinum to reduce impedances to between 160-250 kΩ at 1 kHz. During surgery and before tetrode implantation, several jeweller's screws were placed in the skull. After placing the screws, a layer of OptiBond dental bonding agent (Kerr) and then Charisma® dental filling composite (Kulzer) was applied to the surface of the skull and around the screws. The animals were then simultaneously implanted with two microdrives in the same hemisphere. To prevent the tetrodes from bending and to guide them during deep HDB and PPN implantations, a cannula (30G) was first lowered, at desired medio-lateral and anterior-posterior coordinates and with a 0° angle from vertical, 4.0-5.5 mm ventral to the surface of the brain, for HDB implants, and 3.5-5.0 mm ventral for PPN implants. The guide cannula was left in place for 10 min and then removed. HDB and PPN tetrodes were then placed respectively at 5.0-6.5 mm and 4.0-6.0 mm ventral to the surface of the brain. In MEC, the tetrodes were lowered 1.1-2.2 mm ventral to the surface of the brain in the sagittal plane, with a 20°-24° forward angle compared to vertical. To secure the tetrode implants, a final layer of dental cement was applied. One screw per microdrive was connected to the system ground.

Single unit recordings

Recording experiments took place while the rats foraged in an open field arena (1.5 m x 1.5 m x 50 cm) with black walls and a white rectangular cue card placed on one of the walls. A tall curtain extending from the ceiling to the floor of the room surrounded the recording box except on the side where the animals were placed at the beginning of each recording session. Recording sessions were performed under dim room lighting and lasted a minimum of 20 min, during which the animals chased small chocolate crumbs thrown randomly into the open field to motivate exploration of the whole environment. Single unit activity was collected by connecting microdrive headstages to the multi-unit data acquisition system (Axona Ltd.) via an AC-coupled unity-gain operational amplifier, using a counterbalanced cable that enabled the animals to move freely. Recorded signals were amplified 5,000-15,000 times and band-passed filtered between 0.8 and 6.7 kHz. Triggered spikes were stored to a disk at 48 kHz (50 samples per waveform). An additional video tracking system (Axona Ltd.), connected to the acquisition system, was used to detect a pair of LEDs (one large, one small) attached to the cable of the headstage, and to track the animal's position and head direction throughout the recording session. At the end of each recording session, the tetrodes were advanced a minimum of 50 μm in order to screen new units the following day. A turning log was kept in order to allow future reconstruction of recording sites. In PPN, HDB and MEC, the tetrodes were lowered maximally to respectively 7.85 mm, 8.1 mm, and 4.8 mm ventral to the surface of the brain. The tetrodes were not moved after the final recording session.

Spike sorting

Spike sorting was performed manually using an offline graphical cluster-cutting software (MClust, A.D. Redish). Clustering was initially performed based in two-dimensional projections of waveform amplitude, energy, and the first principal component (Figure S2). Autocorrelation analysis was used to remove single units with more than 1% of spikes during the refractory period. Re-sampled units were manually removed by visual inspection of clusters across multiple recording days. To ensure the assessment of optogenetically-driven responses in the same single units recorded during baseline screening sessions, baseline cluster convex hulls were reapplied to spiking data from stimulation sessions and readjusted in case of slight movement of the clusters.

Optogenetic stimulation

Using similar coordinates as for tracer injections, animals were unilaterally injected with 500-1500 nl of AAV5-CaMKIIa-hChR2(H134R)-EYFP (Karl Deisseroth stock, UNC Vector Core) in PPN (n = 17) or HDB (n = 1). The virus was injected at one (max. 1000 nl) or two sites (max. 750 nl per site), using pulled borosilicate glass pipettes (World Precision Instruments) mounted on a motorized microinjection controller (Nanoliter 2010, World Precision Instruments) at short pulses of 50 nl/pulse, delivered

30 s apart. After each injection the pipette was left in place for an additional 10 min before being retracted. During the same surgery, or in a separate surgery 3-5 weeks later, a fiber-optic cannula was implanted in PPN or HDB (11 mm long, 250 μm outer diameter, MFC_200/245-0.53_11mm_ZF2.5(G)_FLT, Doric Lenses), and tetrode drives were implanted ipsilaterally in HDB and/or MEC. The fiber had been etched in advance by emersion in 4% hydrofluoric acid for 2.5 h. To provide a control for the effects of PPN optogenetic stimulation in locomotion, a similar procedure was used in a different cohort of animals (n = 4) where PPN was injected with a control virus that did not express ChR2, AAV5-CaMKIIa-EYFP (Karl Deisseroth stock, UNC Vector Core), after which the animals were implanted with an optic fiber in PPN. Injections with the ChR2-expressing virus provided strong labeling of axonal processes, but this came at the expense of clear identification of infected neuronal somas, even at higher magnifications. Furthermore, somatic labeling was disguised by the extensive efferent connections of infected PPN cells. By contrast, injections of the control viral vector provided fairly clear somatic labeling of infected neurons in PPN (possibly because cytoplasmic signaling was more homogeneous between neuronal soma and axonal projections than in ChR2-expressing cells), allowing a more unambiguous delineation of infected regions. We therefore used these control injections as a proxy for the assessment of virus spread in the brain of animals used in optogenetic manipulation experiments.

Optogenetic stimulation in PPN and HDB was achieved by connecting the fiber-optic cannula to a 473 nm laser (Shanghai Laser & Optics Co.), via a mono fiber-optic patch cord (MFP_200/230/3000-0.48_8m_SMA_ZF2.5(F), Doric Lenses). To prevent light dispersion during optogenetic stimulation, mating sleeves with opaque black covering were used (SLEEVE_ZR_2.5_BK, Doric Lenses) and carbon powder (484164, Sigma-Aldrich) was added to the dental cement to color it black. Laser stimulation sessions were performed in the open field, after baseline recording sessions, lasting a minimum of 10 min. The stimulation protocol consisted of 5 s long trains of 10 ms laser pulses at 10 Hz frequency (laser trial = 100 ms: 10 ms ON, 90 ms OFF) with 15 s breaks between pulse trains. Pulses were controlled by a mechanical shutter (LS3S2T1 Uniblitz shutter system, Vincent Associates). Output laser power for soma stimulation in PPN/HDB and for stimulation of PPN axonal terminals in HDB were respectively set to 5-10 mW and 10-20 mW, measured at the end of the fiber-optic patch cord connecting to the animal. Temporal control of the mechanic shutter was achieved with a microcontroller running a custom-written routine (Arduino UNO, Arduino). The controller of the shutter was connected to the electrophysiology recording system to provide TTL pulses corresponding to laser stimulation timestamps.

Laser-response analysis

Raster plots of single unit spiking activity, aligned to laser stimulation (−20 ms before to 80 ms after photostimulation onset, in 1 ms bins), were used to build peri-stimulus time histograms (PSTHs) of firing rate for each unit recorded during stimulation sessions. PSTHs were constructed with reference to every single light pulse during 10 Hz trains of stimulation (2071.9 ± 44.0 pulses per experiment, averaged across all optogenetic experiments). Units with an average firing rate below 1 Hz during the 20 ms baseline stimulation period were removed from further analysis given the difficulty of discerning periods of low activity from actual inhibition. To classify stimulation-responsive units, we used a sliding window approach with 10 ms bins and 1 ms increments, starting from laser onset (0 ms), to identify the first 10 ms epoch that across light pulses (i) displayed a significant absolute increase or decrease in firing rate (with a stringent criterion of $p < 0.0001$, Wilcoxon rank-sum test) compared to the baseline average firing rate (−20 to 0 ms), and (ii) displayed a sequence of at least three consecutive bins where firing rate remained above/below the maximum/minimum baseline firing rate. These significance criteria were employed to detect robust and reliable changes in firing rate and to prevent the incorrect classification of sudden and stochastic changes in firing rate as stimulation induced-responses, which we considered particularly important in the case of cells with low and variable firing rates during peri-stimulation epochs. The cell's response latency was defined as the first temporal bin of the sequence of three consecutive bins within the identified 10 ms epoch, where firing rate remained above/below the maximum/minimum baseline firing rate. For units with both positive and negative response windows (e.g., rebound excitation after transient inhibition), the epoch with the shortest latency was used to classify the unit as excited or inhibited.

Speed modulation

The speed modulation of each single unit recorded in PPN, HDB and MEC was computed based on a correlation between single unit firing rate and the animal's locomotion speed (Kropff et al., 2015). Single unit firing rate was obtained by smoothing the vector of spike trains with a 0.4 s Gaussian kernel. For speed calculations, animal position estimates were first inferred by tracking the LEDs attached to the drive's headstage. Speed was computed independently in the *x* and *y* direction by calculating changes in *x* and *y* position for each temporal bin of 20 ms, and then smoothing them with a 0.8 s smoothing window (MATLAB's smoothing function with a "lowess" method, a local regression using weighted linear least-squares and a 1^{st} degree polynomial model). Running speed was then found as the combination of speed in the *x* and *y* direction. Rats ran at speeds ranging up to 52 cm/s (99^{th} percentile) for short periods, with mean running speeds (± SEM) of 14.3 ± 0.09 cm/s across all recording sessions. Speed tuning curves were obtained for each recorded unit by computing histograms of spike counts by temporal coverage of each 10 ms speed bin between 0 cm/s and 50 cm/s. Before computing each unit's speed modulation, a speed filter was applied to limit the analysis of neural data to periods with locomotion speed between 6 cm/s and the mean value of the last 10 cm/s speed bin in which the animal had spent more than 30 s (depending of each trial's speed coverage, these values varied between 35 and 65 cm/s). The lower speed cut-off, modified from a previous report (Kropff et al., 2015), was determined after plotting the average normalized speed tuning curve for all cells recorded in MEC. Two distinct regimes were detected: a steeper linear modulation at low speeds, that could be related to a change in

network state during locomotion onset, and a more gradual linear increase in firing rate for higher speeds (Figure S3A). The transition between these two regimes in MEC occurred around 6 cm/s. A similar breaking point in the speed-rate relationship was also observed in PPN and HDB. We thus applied this lower speed cut-off to all brain areas, removing data below 6 cm/s and eliminating the potential effect of state-dependent network changes in neuronal coding (Ye et al., 2018). After applying the speed filter, the value of each single unit speed modulation was found by computing the Pearson's correlation between firing rate and the animal's filtered speed. In complementary analyses, and in order to compare speed cell classification under linear and non-linear assumptions, we also computed the Spearman's correlation between firing rate and the animal's speed (for epochs with a minimum speed of 6 cm/s; Figure S3B).

To analyze temporal biases in speed coding we applied temporal shifts to each unit's firing rate (20 ms bins, from −1000 ms to 1000 ms) and then correlated each temporally shifted dataset with the animal's running speed to determine, for each unit, the temporal bin in which speed correlation was maximized (or minimized, in the case of negative speed cells). We then computed, for each temporal shift bin, the average speed correlation value for the whole population of recorded units and used this distribution to interpolate the temporal shift that maximized (or minimized) speed correlation values.

Distinction between putative principal cells and interneurons

MEC units were classified as putative principal cells (pPC) and putative interneurons (pINT) based on previously used firing rate and spike width criteria (Frank et al., 2001; Kropff et al., 2015; Tanke et al., 2018; Ye et al., 2018). Spike waveforms for each tetrode channel were peak-aligned and the average waveform on the most prominent channel was used to compute spike width as the time interval between the peak and the trough of the waveform. The collection of spike widths in MEC displayed a bimodal distribution with an average between peaks of ∼240 μs, which was then used as a spike width threshold. A firing rate threshold was set at 10 Hz. Units with spike widths > 240 μs and firing rates < 10 Hz were classified as pPC, whereas the remaining units were classified as pINT.

To assess if differences in firing rate between pPC and pINT in MEC could bias the detection of optogenetic responses, we compared the number of responsive pPC and pINT after randomly downsampling spike occurrences in pINT by a factor of 10 (deletion of 90% of spikes of pINT showing firing rates above 10 Hz during the baseline session), which brought the firing rate of pINT during the stimulation baseline period down to values close to those of pPC (pPC: 3.0 ± 0.1 Hz; pINT: 3.4 ± 0.2 Hz, with only 8 out of 148 pINT still showing stimulation baseline firing rates above 10 Hz after downsampling). The number of responsive pINT remained significantly higher than that of responsive pPC (pPC: 16/206; pINT: 24/148; $Z = 2.5$, $p = 0.01$, two proportions Z-test). The high proportion of speed-modulated cells among responsive pINTs is consistent with the predominance of fast-spiking neurons in the general population of MEC speed cells previously reported (Hinman et al., 2016; Ye et al., 2018). For comparison, in HDB there was no difference in the fraction of responsive pPC and pINT (12 of 16 and 100 of 146, respectively, $Z = 0.5$, $p = 0.6$, two proportions Z-test). These results support the idea that the difference in responsiveness among pPC and pINT in MEC is not related merely to the difference of firing rate in these two neuron populations.

Spatial tuning curves

For the characterization of spatially modulated units, animal position estimates and the relative placement of the LEDs on the drive's headstage were used to respectively compute spatial rate maps and head direction tuning curves for MEC units. Spatial analyses were limited to time epochs in which the animal was moving above 2 cm/s. Rate maps and angular tuning curves were first calculated based on distributions of the ratio between spike counts and time spent in each bin (bin size 4 cm for spatial maps, 6° for head direction), and then smoothed with a Gaussian kernel (σ: 1.5 bins for spatial maps, 1 bin for head direction tuning curves). Grid, head direction and border scores were then calculated based on the resulting rate maps.

Grid score

The grid score for each cell was determined from a series of expanding circular samples of the autocorrelogram, each centered on the central peak but with the central peak excluded (Sargolini et al., 2006; Langston et al., 2010). The radius of the central peak was defined as either the first local minimum in a curve showing correlation as a function of average distance from the center, or as the first incidence where the correlation was under 0.2, whichever occurred first. The radius of the successive circular samples was increased in steps of 1 bin (4 cm). For each sample, we calculated the Pearson correlation of the ring with its rotation in α degrees first for angles of 60° and 120° and then for angles of 30°, 90° and 150°. We then defined the minimum difference between any of the elements in the first group (60° and 120°) and any of the elements in the second (30°, 90° and 150°). The cell's grid score was defined as the highest minimum difference between group-1 and group-2 rotations in the entire set of successive circular samples.

Head direction score

A unit's head direction score was defined as the mean vector length of each single unit's angular tuning curve (Langston et al., 2010). From each single unit's angular tuning curve, if bin i, with orientation θ_i, in radians, is associated with firing rate λ_i, the mean vector length was defined as

$$\left| \frac{\sum \lambda_i e^{i\theta_i}}{\sum \lambda_i} \right|$$

where the sums were performed over all N directional bins and the modulus of the resulting complex number was obtained.

Border score

Border score was defined as the difference between the maximal length of a wall touching on any single firing field of the cell and the average distance of the field from the nearest wall, divided by the sum of those values (Solstad et al., 2008). The range of border scores was thus −1 to 1. Firing fields were defined as collections of neighboring pixels with firing rates higher than 20% of the cell's peak firing rate and a size of at least 200 cm^2.

Shuffling of spike data

Classification of unit functional cell types was performed based on spike data shuffling procedures. For each recorded unit, a total of 100 random temporal shifts were applied to shuffle the sequence of spike data along the animal's path, between 15 s and the total trial length minus 15 s, with the end of the session wrapped to the beginning. For speed calculations in PPN, HDB and MEC, shuffling procedures were computed independently for each brain region, and units were classified as positive or negative speed cells if their speed modulation value was respectively above or below the 99^{th} and 1^{st} percentile of the distribution of shuffled speed modulation values. These percentiles were chosen in order to avoid false positives and limit our analyses to the cells that, among a population with a wide distribution of speed scores, show the strongest linear relationship with running speed and thus represent the most robust expression of ongoing locomotion within PPN, HDB and MEC. Positive and negative speed modulation thresholds - initially computed based on units recorded within the defined anatomical borders of PPN, HDB and MEC - were used to classify speed cells recorded in their respective neighboring regions. The same shuffling procedures were applied to classify speed cells following calculation of speed scores under non-linear assumptions. In MEC, units were classified as grid cells, head-direction cells or border cells if their respective score passed the 99^{th} percentile of a distribution of all shuffled grid, head-direction or border values. For the analysis of how different entorhinal cell classes respond to brainstem optogenetic stimulation, cells with conjunctive properties – crossing shuffling thresholds for more than one functional class - were included in analyses for each of these cell classes (e.g., a cell with grid and head-direction function was analyzed both as a grid cell and as a head-direction cell).

Histological procedure for determining tetrode recording sites

All experimental subjects were euthanized by isoflurane anesthesia, followed by intraperitoneal overdose injection of pentobarbital. Following transcardial perfusion with 0.9% saline and 4% formalin, brains were extracted and stored in 4% formalin until further use. Brains were frozen and sliced in sagittal or coronal sections (30-50 μm) using a cryostat and mounted onto gelatin-covered glass slides, for identification of tetrode tracks, or split in series and collected into well plates with phosphate buffer saline (PBS 0.01 M), for immunohistochemistry. Given the rich cholinergic populations in PPN and HDB, tetrode tracks in these areas were visualized against an acetylcholinesterase (AChE) counterstaining (Tago et al., 1986) to allow identification of their approximate anatomical borders. Briefly, PPN and HDB sections were first rinsed 3 × 10 min in 0.125 M phosphate buffer, and then 3 × 10 min in 0.1 M Maleate buffer (1.6% sodium hydrogen malate). After, the sections were incubated for 30-60 min in Acetylthiocholine solution (10.0 mg Acetylthiocholine Iodide, 1.6 mg Potassium hexacyanoferrate (III), 4.7 mg Copper (II) sulfate, 14.7 mg Natriumcitrat-dihydrate in 100 mL Maleate buffer, pH 5.7/5.8), at room-temperature and in the dark, and then rinsed 2 × 5 min in a 0.05 M Tris-HCl buffer. Finally, the sections were incubated in 0.04% 3,3′-Diaminobenzidine (DAB) in Tris-HCl, until the appearance of a distinct brown coloration in cholinergic-rich areas, and then washed 2 × 5 min in a Tris-HCl buffer to stop DAB reaction. In the event of unclear staining, identification of PPN and HDB was achieved with complimentary choline acetyltransferase (ChAT) immunofluorescence staining in an adjacent series of sections. For MEC sections, tetrode tracks and anatomical borders were identified with cresyl violet staining.

Reconstruction of tetrode recording sites

Photomicrographs of PPN, HDB, and MEC sections with the deepest tetrode position were obtained with a digital camera mounted on a bright-field microscope, and length of tetrode tracks were measured with ZEN Blue (Zeiss). These measurements, and the readout from the tetrode turning log, were used to extrapolate a reconstruction of every recording site, onto which the approximate position of relevant anatomical borders of PPN (dorsal and ventral), HDB (dorsal) and MEC (dorsal) was mapped. The recording depth of all units recorded in PPN and HDB, as well as surrounding dorsal and ventral regions, was then expressed with respect of the dorsal boundary of PPN and HDB, respectively. In the case of MEC, the position of each unit was projected onto flat maps and expressed with reference to the dorsal MEC boundary (Giocomo et al., 2014). All units recorded dorsal or ventral to the anatomical borders of each target regions, as well as units recorded in subjects where our tetrode implants missed the target area, were classified as off-target units. A cell was not considered off-target unless it was more than 50 μm away from the border of the target region, in order to rule out cross-border volume conduction of unit signals[77]. Off-target regions included the mesencephalic reticular formation dorsal and ventral of PPN, the nucleus accumbens, ventral pallidum, substantia innominata, and preoptic area dorsal and caudal to HDB, and the retrosplenial and perirhinal cortices and pre and parasubiculum dorsal and rostral of MEC. Cells from these regions were only included in the analysis of differences in proportion of speed cells and speed modulation between each target area and their respective off-target regions (Figure S4). To analyze the anatomical distribution of speed cells recorded throughout the brainstem, basal forebrain, and entorhinal cortex, we divided the entire length of screened tissue into bins of 200 μm and then calculated the percentage of speed cells among all recorded units for each bin (positive and negative speed cells of all animals grouped together).

Immunohistochemistry and imaging

Series of sagittal sections spanning the full medio-lateral extent of the brain were stained to confirm FB and BDA injection sites in MEC and PPN, respectively, and for brain-wide identification of regions showing conspicuous co-expression of FB and BDA staining. A first series of sections was rinsed 3 × 10 min in PBS-T (0.01M PBS with 0.3% Triton X-100), followed by preincubation for 2 h with a blocking solution (PBS-T, with 3% normal donkey serum (NDS)). Sections were then incubated with streptavidin-Alexa Fluor 546 (1:200 in PBS-T, S11225, ThermoFisher Scientific) for 2 h at room temperature, rinsed 2 × 5 min in PBS, and mounted with ProLong diamond antifade mounting medium (P36965, ThermoFisher Scientific). Fluorescent Nissl deep red 640/660 (1:200 in PBS, N-21483, NeuroTrace, ThermoFisher Scientific) was added after streptavidin incubation to provide anatomical contrast between brain regions. To further confirm BDA injection site in PPN and assess the extent of co-expression of FB and BDA in cholinergic-rich areas, an adjacent series of sections was processed for BDA staining and for choline acetyltransferase (ChAT) immunostaining.

For ChAT and YFP immunohistochemistry sections were rinsed for 3 × 10 min in 0.01 M PBS-T and preincubated for 2 h with a blocking solution (PBS-T, with 3% NDS). Next, sections were incubated overnight at 4°C with primary antibodies, rabbit anti-GFP (1:1000, A1112, ThermoFisher Scientific) and goat anti-ChAT (1:500, AB144P, Merck Millipore) in blocking solution. Next, the sections were rinsed for 3 × 10 min in PBS-T and incubated with the secondary antibodies, donkey anti-rabbit Alexa Fluor 488 (1:1000, A21206, ThermoFisher Scientific) and donkey anti-goat Alexa Fluor 568 or Alexa Fluor 647 (1:1000, A11057/A21447, ThermoFisher Scientific) in blocking solution, for 2 h at room temperature. Finally, the sections were washed 2 × 5 min in PBS and mounted with Prolong mounting medium. To assess virus expression in PPN, 4 sections at defined medio-lateral levels were selected per animal, based on anatomical reference points and compared to the rat brain atlas (Paxinos and Watson, 2007). In Photoshop (Adobe), the area of virus expression in each section of each animal was outlined, and the outlines of each medio-lateral level were then aligned and superimposed with 30% transparency (Caggiano et al., 2018). All fluorescent images were collected using a confocal microscope (LSM 880, Zeiss), or scanned on a scanning microscope (Axio Scan.Z1, Zeiss).

QUANTIFICATION AND STATISTICAL ANALYSIS

The experimenters were not blind to subject treatments and no statistical methods were employed to predetermine sample size. Details regarding data distributions, statistical tests and sample size are presented in the main text, figures, and figure legends. Data presented as mean ± standard error of the mean (SEM), unless otherwise specified. All data was analyzed with custom-written MATLAB scripts (https://se.mathworks.com/). Nonparametric tests were used to analyze data violating normal distribution assumptions (Kolmogorov-Smirnov test), and all statistical tests performed were two-tailed with significance level set at $p < 0.05$. For detection of optogenetic responses significance level was set at $p < 0.0001$.